



**NAVAL  
POSTGRADUATE  
SCHOOL**

**MONTEREY, CALIFORNIA**

**THESIS**

**MESOSCALE VARIABILITY IN COASTAL  
STRATOCUMULUS CLOUDS OBSERVED DURING  
UPPEF2012**

by

Kyle B. Franklin

March 2014

Thesis Advisor:  
Second Reader:

Qing Wang  
Wendell Nuss

**Approved for public release; distribution is unlimited**

THIS PAGE INTENTIONALLY LEFT BLANK

<b>REPORT DOCUMENTATION PAGE</b>			<i>Form Approved OMB No. 0704-0188</i>	
Public reporting burden for this collection of information is estimated to average 1 hour per response, including the time for reviewing instruction, searching existing data sources, gathering and maintaining the data needed, and completing and reviewing the collection of information. Send comments regarding this burden estimate or any other aspect of this collection of information, including suggestions for reducing this burden, to Washington headquarters Services, Directorate for Information Operations and Reports, 1215 Jefferson Davis Highway, Suite 1204, Arlington, VA 22202-4302, and to the Office of Management and Budget, Paperwork Reduction Project (0704-0188) Washington DC 20503.				
<b>1. AGENCY USE ONLY (Leave blank)</b>		<b>2. REPORT DATE</b> March 2014	<b>3. REPORT TYPE AND DATES COVERED</b> Master's Thesis	
<b>4. TITLE AND SUBTITLE</b> MESOSCALE VARIABILITY IN COASTAL STRATOCUMULUS CLOUDS OBSERVED DURING UPPEF2012			<b>5. FUNDING NUMBERS</b>	
<b>6. AUTHOR(S)</b> Kyle B. Franklin				
<b>7. PERFORMING ORGANIZATION NAME(S) AND ADDRESS(ES)</b> Naval Postgraduate School Monterey, CA 93943-5000			<b>8. PERFORMING ORGANIZATION REPORT NUMBER</b>	
<b>9. SPONSORING /MONITORING AGENCY NAME(S) AND ADDRESS(ES)</b> N/A			<b>10. SPONSORING/MONITORING AGENCY REPORT NUMBER</b>	
<b>11. SUPPLEMENTARY NOTES</b> The views expressed in this thesis are those of the author and do not reflect the official policy or position of the Department of Defense or the U.S. Government. IRB protocol number ___N/A___.				
<b>12a. DISTRIBUTION / AVAILABILITY STATEMENT</b> Approved for public release; distribution is unlimited			<b>12b. DISTRIBUTION CODE</b> A	
<b>13. ABSTRACT (maximum 200 words)</b> <p>Analysis of satellite imagery shows horizontally extensive coastal stratocumulus layers with closed cell mesoscale cellular convection (MCC) near the coast transitioning to open cell MCC further offshore. The nearshore MCC region had a dominant length scale of 8.5 km. The offshore open cell region had larger length scales of 12 km to 20 km.</p> <p>Aircraft transects conducted through the closed cell MCC exhibited variable perturbations on two distinct length scales. Perturbations associated with MCC occurred at lengths scales identical to satellite observations. Perturbations also occurred on smaller length scales due to narrow, sub-kilometer convective downdraft events imbedded within the MCC. These events showed less spatial organization than MCC, with the distance between events ranging from .5 km to 3 km, and typical event widths of 1 km or less. Typical event perturbations include colder, dryer, downdrafts.</p> <p>Analysis of dynamic and thermodynamic variables has shown that typical downward velocities of .25 ms-1 exist in the middle of the cloud layer, but subsequent horizontal mixing of adjacent air reduces the magnitude of thermodynamic perturbations in the downdrafts, reduces negative buoyancy, and slows the downdraft near cloud base. These narrow downdraft events are a significant source of boundary layer vertical temperature and moisture fluxes.</p>				
<b>14. SUBJECT TERMS</b> Stratocumulus clouds, mesoscale variability, mesoscale cellular convection, UPPEF 2012, aircraft measurements.			<b>15. NUMBER OF PAGES</b> 83	
			<b>16. PRICE CODE</b>	
<b>17. SECURITY CLASSIFICATION OF REPORT</b> Unclassified	<b>18. SECURITY CLASSIFICATION OF THIS PAGE</b> Unclassified	<b>19. SECURITY CLASSIFICATION OF ABSTRACT</b> Unclassified	<b>20. LIMITATION OF ABSTRACT</b> UU	

THIS PAGE INTENTIONALLY LEFT BLANK

**Approved for public release; distribution is unlimited**

**MESOSCALE VARIABILITY IN COASTAL STRATOCUMULUS CLOUDS  
OBSERVED DURING UPPEF2012**

Kyle B. Franklin  
Lieutenant, United States Navy  
B.S., United States Naval Academy, 2005

Submitted in partial fulfillment of the  
requirements for the degree of

**MASTER OF SCIENCE IN METEOROLOGY AND PHYSICAL  
OCEANOGRAPHY**

from the

**NAVAL POSTGRADUATE SCHOOL  
March 2014**

Author: Kyle B. Franklin

Approved by: Qing Wang  
Thesis Advisor

Wendell Nuss  
Second Reader

Wendell Nuss  
Chair, Department of Meteorology

THIS PAGE INTENTIONALLY LEFT BLANK

## ABSTRACT

Analysis of satellite imagery shows horizontally extensive coastal stratocumulus layers with closed cell mesoscale cellular convection (MCC) near the coast transitioning to open cell MCC further offshore. The nearshore MCC region had a dominant length scale of 8.5 km. The offshore open cell region had larger length scales of 12 km to 20 km.

Aircraft transects conducted through the closed cell MCC exhibited variable perturbations on two distinct length scales. Perturbations associated with MCC occurred at lengths scales identical to satellite observations. Perturbations also occurred on smaller length scales due to narrow, sub-kilometer convective downdraft events imbedded within the MCC. These events showed less spatial organization than MCC, with the distance between events ranging from .5 km to 3 km, and typical event widths of 1 km or less. Typical event perturbations include colder, dryer, downdrafts.

Analysis of dynamic and thermodynamic variables has shown that typical downward velocities of  $.25 \text{ ms}^{-1}$  exist in the middle of the cloud layer, but subsequent horizontal mixing of adjacent air reduces the magnitude of thermodynamic perturbations in the downdrafts, reduces negative buoyancy, and slows the downdraft near cloud base. These narrow downdraft events are a significant source of boundary layer vertical temperature and moisture fluxes.

THIS PAGE INTENTIONALLY LEFT BLANK

# TABLE OF CONTENTS

<b>I.</b>	<b>INTRODUCTION.....</b>	<b>1</b>
	<b>A. IMPORTANCE OF STRATOCUMULUS CLOUDS.....</b>	<b>1</b>
	<b>B. STRATOCUMULUS AND MILITARY OPERATIONS .....</b>	<b>2</b>
	<b>C. THESIS OBJECTIVES.....</b>	<b>3</b>
<b>II.</b>	<b>BACKGROUND .....</b>	<b>5</b>
	<b>A. THE STRATOCUMULUS TOPPED BOUNDARY LAYER .....</b>	<b>5</b>
	<b>B. PHYSICAL PROCESSES CONTROLLING STRATOCUMULUS MESOSCALE VARIABILITY .....</b>	<b>7</b>
	<b>1. Physical Processes .....</b>	<b>7</b>
	<i>a. Microphysical Characteristics .....</i>	<i>7</i>
	<i>b. Radiation .....</i>	<i>9</i>
	<i>c. Turbulence .....</i>	<i>10</i>
	<i>d. Entrainment .....</i>	<i>11</i>
	<i>e. Drizzle/Precipitation.....</i>	<i>12</i>
	<b>2. Mesoscale Processes .....</b>	<b>13</b>
	<b>3. Synoptic Scale Processes.....</b>	<b>14</b>
	<b>C. STRATOCUMULUS MESOSCALE VARIABILITY.....</b>	<b>16</b>
	<b>1. Temporal Variability .....</b>	<b>17</b>
	<b>2. Mesoscale Cellular Convection.....</b>	<b>18</b>
	<b>3. Previous MCC Research .....</b>	<b>19</b>
	<b>D. UPPEF MEASUREMENTS OVERVIEW.....</b>	<b>20</b>
	<b>1. Synoptic Summary for RF05 and RF10.....</b>	<b>20</b>
<b>III.</b>	<b>ANALYSIS OF SATELLITE OBSERVED CLOUD STRUCTURE .....</b>	<b>23</b>
	<b>A. UPPEF2012 CLOUD STRUCTURE OVERVIEW.....</b>	<b>23</b>
	<b>B. ANALYSIS OF CLOUD STRUCTURE FROM GOES IRRADIANCE MEASUREMENTS .....</b>	<b>24</b>
	<b>1. Analysis Methodology.....</b>	<b>25</b>
	<b>2. Spatial Variability .....</b>	<b>31</b>
	<i>a. RF05 .....</i>	<i>31</i>
	<i>b. RF10 .....</i>	<i>33</i>
	<b>3. Temporal Variability .....</b>	<b>35</b>
	<i>a. RF05 .....</i>	<i>35</i>
	<i>b. RF10 .....</i>	<i>36</i>
<b>IV.</b>	<b>AIRCRAFT DATA ANALYSIS.....</b>	<b>39</b>
	<b>A. DATA SELECTION METHODOLOGY.....</b>	<b>39</b>
	<b>B. RF05 AIRCRAFT DATA ANALYSIS.....</b>	<b>39</b>
	<b>C. RF10 AIRCRAFT DATA ANALYSIS.....</b>	<b>52</b>
<b>V.</b>	<b>DISCUSSION .....</b>	<b>59</b>
	<b>A. SUMMARY AND CONCLUSIONS .....</b>	<b>59</b>
	<b>B. RECOMMENDATIONS FOR FUTURE RESEARCH.....</b>	<b>60</b>

<b>LIST OF REFERENCES</b> .....	<b>61</b>
<b>INITIAL DISTRIBUTION LIST</b> .....	<b>65</b>

## LIST OF FIGURES

Figure 1.	Typical vertical profiles of water vapor ( $q$ ), liquid water ( $q_l$ ), equivalent potential temperature ( $\theta_e$ ), and temperature ( $T$ ) (from Wood 2012). ....	5
Figure 2.	Various forms of MCC (from Wood 2012). ....	16
Figure 3.	Spatial extent of MCC (from Agee 1987). ....	18
Figure 4.	(a) Sea level pressure and (b) surface vector winds during RF05. ....	21
Figure 5.	(a) Sea level pressure and (b) surface vector winds during RF10. ....	21
Figure 6.	Cloud structure variability during UPPEF 2012. Blue lines indicate approximate flight tracks (from Tellado 1013). ....	24
Figure 7.	Cirrus cloud reflectance during RF05. ....	26
Figure 8.	Cirrus cloud reflectance during RF10. ....	26
Figure 9.	Cloud field from RF05. (a) GOES image and (b) MATLAB generated from GOES data. ....	28
Figure 10.	Same as in Figure 9, except for RF10. ....	28
Figure 11.	Sample GOES Radiance cross section from RF05 closed cell MCC. ....	29
Figure 12.	Illustration of 1-D sampling from the 2-D irradiance field of satellite measurements. ....	30
Figure 13.	Multiple transect averaging process. (a) PSD from individual transects and (b) “area-averaged” PSD from three transects in (a). ....	30
Figure 14.	Nearshore and offshore cross section locations at 1800 GMT. ....	31
Figure 15.	Log-log plots of nearshore (red) and offshore (black) (a) individual cross section PSD and (b) area-averaged PSD. ....	32
Figure 16.	PSD of irradiance for nearshore and offshore region as a function of wavelength. ....	33
Figure 17.	Nearshore and offshore transect locations for RF10. ....	33
Figure 18.	Log-log plots of nearshore (red) and offshore (black) (a) individual cross section PSD and (b) area-averaged PSD. ....	34
Figure 19.	Same as in Figure 16, except for RF10. ....	35
Figure 20.	GOES irradiance (a) two hours prior and (b) two hours after RF05. ....	36
Figure 21.	Area averaged PDS (a) two hours prior and (b) two hours after RF05. ....	36
Figure 22.	GOES irradiance (a) two hours prior and (b) two hours after RF10. ....	37
Figure 23.	Area averaged PSD (a) two hours prior and (b) two hours after RF10. ....	37
Figure 24.	Spatial variations along the flight track observed from RF05 LL1. Shown here are cloud liquid water content ( $q_l$ ), droplet number concentration ( $N_c$ ) and droplet mean effective radius ( $R_e$ ), vertical velocity ( $w$ ), potential temperature ( $\theta$ ), water vapor ( $q$ ), wind speed ( $wspd$ ) and wind direction ( $wdir$ ). ....	40
Figure 25.	Same as in Figure 24, except for LL3 of RF05. ....	41
Figure 26.	Same as in Figure 24, except for RF05, LL8. ....	42
Figure 27.	PSD for RF05 LL1 (a) vertical velocity (b) $\theta$ and (c) $q_l$ . ....	43
Figure 28.	Same as in Figure 27, except for RF05 LL3. ....	43
Figure 29.	Same as in Figure 27, except, for RF05 LL8. ....	43

Figure 30.	Example of cloud break “events” indicated by a green gate function. The original liquid water content is shown in blue, high-pass filtered $q_l$ is shown in red. ....	44
Figure 31.	Event spatial characteristic PDFs for RF05. (a) LL1 and (b) LL3. ....	45
Figure 32.	Event spatial characteristic PDF for RF05 LL8. ....	45
Figure 33.	Event property characteristics for RF05 (a) LL1 and (b) LL3. ....	46
Figure 34.	Event property characteristics for RF05 LL8. ....	46
Figure 35.	Correlation of event properties with event mean vertical velocity for RF05 (a) LL1 and (b) LL3. ....	48
Figure 36.	Variable relationship for RF05 LL8. ....	48
Figure 37.	LL1 wind confluence and vertical wind plot. ....	49
Figure 38.	PSD for wind confluence on LL1. ....	50
Figure 39.	RF05 LL1 Co-spectrum of (a) $w$ and $q_l$ (b) $w$ and $q$ (c) $w$ and $\theta$ . ....	51
Figure 40.	RF05 LL3 Co-spectrum of (a) $w$ and $q_l$ (b) $w$ and $q$ (c) $w$ and $\theta$ . ....	51
Figure 41.	RF05 LL8 Co-spectrum of (a) $w$ and $q_l$ (b) $w$ and $q$ (c) $w$ and $\theta$ . ....	52
Figure 42.	Same as in Figure 24, except for RF10 LL4. ....	52
Figure 43.	Same as in Figure 24, except for RF10 LL5. ....	53
Figure 44.	PSD calculation for RF10, LL4 (a) $q_l$ (b) $w$ , and (c) $\theta$ . ....	53
Figure 45.	PSD calculation for RF10, LL5 (a) $q_l$ (b) $w$ , and (c) $\theta$ . ....	54
Figure 46.	Spatial characteristics for cloud break events in RF10 (a) LL4 and (b) LL5. ....	54
Figure 47.	Event property characteristics for RF10 (a) LL4 and (b) LL5. ....	55
Figure 48.	Variable relationship for RF10 (a) LL4 and (b) LL5. ....	56
Figure 49.	PSD for wind confluence on RF10 (a) LL4 and (b) LL5. ....	56
Figure 50.	RF10 LL4 Co-spectrum of (a) $w$ and $q_l$ (b) $w$ and $q$ (c) $w$ and $\theta$ . ....	57
Figure 51.	RF10 LL4 Co-spectrum of (a) $w$ and $q_l$ (b) $w$ and $q$ (c) $w$ and $\theta$ . ....	58

## LIST OF TABLES

Table 1.	Twin Otter in-cloud level legs investigated.....	39
Table 2.	Correlation coefficients between event averaged vertical velocity and water vapor, $\theta$ , and liquid water and event mean perturbations from each leg.....	48
Table 3.	Correlation coefficients and downdraft perturbation values.....	56

THIS PAGE INTENTIONALLY LEFT BLANK

## LIST OF ACRONYMS AND ABBREVIATIONS

AMTEX	Air Mass Transformation Experiment
BL	boundary layer
BLH	boundary layer height
CIRPAS	Center for Interdisciplinary Remote-Piloted Aircraft Studies
CLASS	comprehensive large array-data stewardship system
CCN	cloud condensation nuclei
CTEI	cloud-top entrainment instability
DMSF	Defense Meteorological Satellite Program
EPAC	Eastern Pacific
EM/EO	electro-magnetic/electro-optic
EIL	entrainment interfacial layer
FIRE	First ISCCP Regional Experiment
GOES	Geostationary Operational Environmental Satellite
IR	infrared
ISR	intelligence, surveillance, reconnaissance
ISCCP	International Satellite Cloud Climatology Project
LAADS	Land and Atmosphere Archive and Distribution System
LHF	latent heat flux
LWC	liquid water content
LWP	liquid water path
LTS	lower tropospheric stability
MBL	marine boundary layer
MODIS	moderate resolution imaging spectroradiometer
NetCDF	network common data form
NCAR	National Center for Atmospheric Research
NCEP	National Centers for Environmental Prediction
NOAA	National Oceanographic & Atmospheric Administration
NRL	Naval Research Laboratory
NSF	National Science Foundation
NIR	near infrared

NWP	numerical weather prediction
NWS	National Weather Service
ONR	Office of Naval Research
PBL	planetary boundary layer
PDF	probability density function
PSD	power spectral density
STAR	Center for Satellite Applications and Research
SHF	sensible heat flux
SLP	sea level pressure
SST	sea surface temperature
STBL	stratocumulus topped boundary layers
STCU	stratocumulus
TFCC	Task Force Climate Change
TIROS	television infrared observation satellite
TKE	turbulent kinetic energy
UPPEF	unified physical parameters for extended forecasts

## **ACKNOWLEDGMENTS**

I would like to thank my thesis advisor, Qing Wang, for her outstanding support and assistance. Mike Cook and Mary Jordan were very helpful with their MATLAB and data processing assistance. Kurt Nielsen assisted with some of the remote sensing data acquisition and calibration. Thanks to my family for the support and inspiration throughout this entire process.

THIS PAGE INTENTIONALLY LEFT BLANK

# I. INTRODUCTION

## A. IMPORTANCE OF STRATOCUMULUS CLOUDS

Stratocumulus clouds (STCU) are low-level clouds that exhibit horizontally homogenous, sheet-like properties of stratus clouds, as well as imbedded convective up and down drafts similar to cumulus clouds. Unlike cumulus clouds, convection within stratocumulus clouds is primarily driven by cloud top cooling, which makes the dynamics controlling convection considerably more complicated, since processes such as radiation and latent processes related to state changes become important (Agee 1987). The dynamic and thermodynamic processes associated with these convective elements largely control the mesoscale spatial variability of stratocumulus clouds, and hence are a major focus in this thesis.

Stratocumulus clouds exist over a large portion of the Earth's surface. According to Warren et al. (1986), stratocumulus clouds occupy approximately one-fifth of the Earth's surface in the annual mean. Additionally, stratocumulus clouds greatly alter the Earth's net shortwave radiation and outgoing long wave radiation. This combination of large spatial extent and strong radiative forcing significantly affects the Earth's radiation balance and energy budget. Over short time scales and on a regional scale, the presence of stratocumulus clouds has a significant effect on the short-term forecasting of low level environmental parameters and phenomena, including air and surface temperatures or fog probabilities and distribution (Nicholls 1983). Over longer time scales, areas of persistent stratocumulus cloud cover greatly control regional climatology (Bergman 1996). When considering the net radiative effects, vastness, and persistence of stratocumulus clouds over long timescales, a significant effect on the Earth's globally averaged albedo and hence climate is likely. Therefore, a thorough understanding of the processes regulating stratocumulus extent and variability becomes an important piece of the global warming puzzle, and a vital objective of the atmospheric sciences (Wood 2012). Mesoscale structures and their associated cloud breaks can play a large role in area-averaged cloud radiative properties, and hence affect the radiation budget.

Most of the dominant dynamic and thermodynamic processes occurring within stratocumulus clouds (turbulent mixing, condensation, evaporation, and radiation) occur on spatial and timescales that are not currently resolvable by numerical weather prediction models. Since these processes cannot be directly modeled, they must be parameterized in order to emulate their net effects on the modeled environment. Therefore, a thorough understanding of the processes involved in stratocumulus clouds is necessary to properly parameterize these sub-grid scale processes and improve model performance. Despite the aforementioned significance of stratocumulus clouds, details of the dynamic and thermodynamics processes occurring within them are still not completely understood.

## **B. STRATOCUMULUS AND MILITARY OPERATIONS**

A change in the Earth's climate is a long-term concern for the U.S. Navy. Task Force Climate Change (TFCC) was created by the Chief of Naval Operations in 2009 to refine the Navy's future role and response to an uncertain future climate ("Climate Change" 2009). The radiative effects of stratocumulus clouds play a pivotal role in the complicated feedback process in the global climate system. Consequently, improvements in the representation of stratocumulus clouds in climate models have been one of the research foci of many Navy sponsored research initiatives.

The Navy is very reliant on atmospheric and oceanographic models in order to conduct aircraft and ship operations in a safe manner. A better understanding of subgrid-scale processes occurring within stratocumulus clouds will improve forecast models via refining model parameterizations. These improvements also have implications for conventional satellite based intelligence, surveillance, reconnaissance (ISR) operations, since extensive stratocumulus layers are a hindrance to detecting enemy assets, or an advantage in obscuring our assets.

Many of the Navy's fleet concentration areas, including Naval Station San Diego are located within areas of persistent stratocumulus cover. Stratocumulus cover persists over the west coasts of major continents out to 1000 km, an area the Navy commonly operates. For this reason, improved knowledge of stratocumulus variability has great

implications for naval surface operations and naval flight operations. The short term radiative effects caused by the presence or absence of stratocumulus clouds plays a large role in distribution and evolution of near-surface, sensible weather. For this reason, stratocumulus clouds directly and strongly affect the operating environment that personnel and equipment are exposed to.

The transmission of electro-magnetic/ electro-optic (EM/EO) energy is strongly dependent on low-level atmospheric temperature and humidity. Atmospheric ducts refract and concentrate propagating energy in a manner that can significantly increase range. Surface ducts are very closely associated with strong and shallow boundary layer inversions, conditions, which are also favorable for persistent stratocumulus regions (Engeln and Teixeira 2004). Therefore, these ducts, and the atmospheric conditions that favor them, are of great importance for radio and radar transmission related to naval operations.

### **C. THESIS OBJECTIVES**

My thesis research will focus on mesoscale variability in the stratocumulus-topped boundary layer (STBL). During Unified Physical Parameters for Extended Forecasts 2012 (UPPEF 2012), a variety of distinct mesoscale structures and organization were observed over relatively small spatial regions. Observed cloud structures include: solid stratocumulus sheets, open and closed cellular convection, rift areas, and linear row structures (horizontal roll vortices).

Specifically, this research will focus on mesoscale cellular convection due to the large amount of data collected from level line transects through these features, when compared to the other cloud features. Using satellite observations and concurrent aircraft measurements, the evolution of mesoscale features with increasing distance from the coast will be examined. Both the temporal and spatial variability of mesoscale cellular convection will be examined through an analysis of satellite imagery. Then, in-situ aircraft measurements will be analyzed and compared to the satellite data at identical

time and place. Composites of this data will be used to draw inferences about the microphysical, macro physical, dynamic, and thermodynamic processes occurring within the STBL, particularly on mesoscales.

## II. BACKGROUND

### A. THE STRATOCUMULUS TOPPED BOUNDARY LAYER

Stratocumulus clouds require specific environmental conditions in order to form and persist. Therefore, a basic understanding of STBL dynamic and thermodynamic structure, as shown in Figure 1, is a prerequisite to understanding stratocumulus evolution and variability.

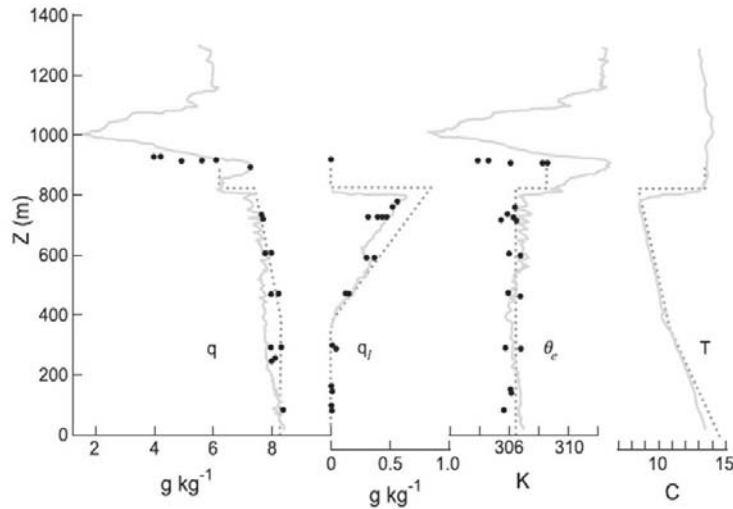


Figure 1. Typical vertical profiles of water vapor ( $q$ ), liquid water ( $q_l$ ), equivalent potential temperature ( $\theta_e$ ), and temperature ( $T$ ) (from Wood 2012).

In the sub-cloud layer, air temperatures decrease at the dry adiabatic lapse rate. Once saturation at cloud based is reached at the lifting condensation level, the lapse rate decreases to the moist adiabatic lapse rate due to latent heat release. At the cloud top, a strong temperature inversion exists. Liquid water ( $q_l$ ) increases quazi-linearly within the cloud as condensation occurs. Water vapor ( $q$ ) is somewhat constant with height below the cloud, and decreases within the cloud as water vapor condenses to liquid water.

The well mixed nature of this layer ensures that conserved variables involving phase change of water substance are independent of height in the non-precipitating

STBL. For example, equivalent potential temperature and specific total water content are conserved (Nicholls 1983) as evaporation and condensation occur within the STBL, a thermodynamic process known as the pseudo-adiabatic process. Total water is conserved with height as the linear increase of  $q_t$  with height is balanced by an equivalent decrease in  $q$ . Specifically, the rate of increase of  $q_t$  with height is often benchmarked against the adiabatic liquid water profile, which is an idealized and theoretical maximum rate of increase with height of this variable. Stratocumulus clouds can exhibit significant departures from the adiabatic liquid water content near the cloud top due to processes that reduce liquid water content within the cloud. These processes include dry air entrainment and subsequent evaporation, or significant precipitation and drizzle. The vertically integrated liquid water content is defined as the liquid water path (LWP) of the cloud. Setting a ratio of a clouds' LWP to the idealized adiabatic-case LWP, defines the term adiabaticity ( $F_{ad}$ ).

One of the necessary atmospheric conditions for sustained stratocumulus clouds is a strong temperature inversion maintained by large-scale subsidence under the subtropical high pressure system. The stable stratification of the inversion air provides an upper limit to cloud growth into higher levels. Very often, part of the inversion and below is also identified as the entrainment interfacial layer (EIL), the region with significant entrainment mixing occurring at the interface of the cloud top and free atmosphere. Nicholls and Leighton (1985) noted that the properties of air at the top of the cloud layer and the overlying inversion are usually so different and the thickness of the layer between them so small that the transition is often well represented by a discontinuity. Specifically, temperature increases at the inversion may exceed one degree kelvin per meter (Wood 2012), and profiles of  $q$  and  $q_t$  decrease rapidly, which drives a decrease in equivalent potential temperature. The primary physical mechanisms responsible for stratocumulus convection, such as radiative cooling and entrainment, occur at the cloud top/EIL interface. The resulting evaporative cooling and long-wave radiational cooling form convective downdrafts and maintain the strong temperature inversion via cooling the lower portion of the EIL. Since the EIL is a thin interface separating the underlying stratocumulus layer and the overlying free atmosphere, its thermodynamic properties can

be seen as a mixture of the adjacent layers, and are thereby highly spatially variable, depending on local entrainment and convective mixing processes.

## **B. PHYSICAL PROCESSES CONTROLLING STRATOCUMULUS MESOSCALE VARIABILITY**

Stratocumulus clouds have convective circulations that are very organized and result from processes occurring at turbulent (10m–1km) and mesoscale (1–10 km) spatial scales (Stevens et al. 2005). For this reason, any study of the organization and structure of stratocumulus clouds must begin with an understanding of the physical processes involved in the STCU boundary layer.

The evolution of stratocumulus clouds depends upon the effect of physical processes occurring on a wide range of scales (Nicholls 1983). In order to understand the reasons for mesoscale variability, we must consider the net effects of physical processes occurring on a variety of physical scales. The dynamic processes governing the spatial variability of stratocumulus clouds are largely invisible to the human eye, only when liquid water ( $q_l$ ) is condensed do we have a visual tracer to assist with a conceptual understanding of the processes involved. The study of mesoscale features and dynamics are interrelated.

### **1. Physical Processes**

Nicholls (1983) noted that a combination of localized, macroscale processes occurring within stratocumulus clouds are primary mechanism forcing turbulent mixing processes, and subsequent larger scale convective motions. The primary microscale and macroscale processes occurring within STCU are described in this section.

#### ***a. Microphysical Characteristics***

The microphysical properties and associated microphysical processes of individual liquid water droplets collectively contribute to important larger scale stratocumulus dynamical processes. Specifically, as noted by Wood (2012), the mean cloud droplet size ( $R_e$ ) and cloud droplet concentration ( $N_d$ ) have important implications for stratocumulus albedo, and hence radiative properties, as well as thermodynamic and

dynamic effects related to latent heating and cooling as well as precipitation. Martin et al. (1994) noted that cloud droplet concentration is highly dependent upon the availability of cloud condensation nuclei (CCN). The process by which water vapor condenses upon CCN to form a water droplet (liquid water) is known as droplet activation. Droplet activation, and hence  $N_d$ , is dependent upon several factors. Twomey (1959) noted that large vertical velocities, often found in convective cells, can lead to an increase in droplet activation, resulting in increased  $N_d$ . Also, Abdul-Razzak et al. (1998), showed that a correlation between  $N_d$  and both the radius and concentration ( $N_1$ ) of CCN exists.

Specifically, the condensation of moisture within rising air parcels and evaporation from falling drizzle and dry air entrainment are the primary mechanisms governing vertical variations in cloud microstructure within stratocumulus clouds, and represents a major heat source and sink within the STBL due to latent heating and cooling processes. Aircraft studies by Slingo et al. (1982) and Nicholls (1983) concluded that a quazi-linear increase of  $q_l$  with height is due primarily to an increase in the mean volume radius ( $r_v$ ), rather than an increase in concentration.

At the cloud top, entrainment of unsaturated air evaporates water droplets (Nicholls and Leighton 1985), which acts to reduce the droplet concentration rather than reduce the mean size of the drops. Goodman (1977) and Noonkester (1984) noted that CCN characteristics played a large role in water droplet concentration ( $N_d$ ), with clouds developing in typical “maritime” CCN characteristics exhibiting a smaller number of droplets when compared to “continental” STCU with a larger number of CCN.

As condensation continues and droplets get larger, their continued growth predominantly occurs due to the coalescence of adjacent droplets, a process known as autoconversion. As this newly formed drizzle increases in mass and feels the effects of gravity, it falls to earth, colliding with droplets in its’ path and continues to grow, a process known as accretion. For this reason, larger droplets may be observed near the cloud base due to coalescence and gravitational settling. These processes govern the vertical variations in cloud droplet radius. Multiple studies, including that of Bretherton et al. 2004, have shown that increased  $N_d$  inhibits the autoconversion process and results in a reduction of drizzle.

***b. Radiation***

The distribution of liquid water in stratocumulus clouds is the primary factor affecting the optical and radiative properties of the cloud layer. For infrared (IR) wavelengths, the volume absorption coefficient is the primary derived quantity for determining IR energy interaction with the cloud layer; this quantity is proportional to the product of  $q_l$  and a mass absorption coefficient, which is independent of the size of cloud droplets, provided that the droplet radius is much smaller than the IR wavelengths. For this reason, high levels of liquid water result in a large volume absorption coefficient, and relatively short penetration depths, since penetration is inversely proportional to absorption. Indeed, in-situ aircraft radiation flux measurements have shown that net radiative cooling is restricted to a layer approximately 30 m deep at cloud top with modest radiative warming throughout the rest of the cloud (Nicholls 1983). These layers of radiative cooling and warming occur due to a net divergence and convergence of IR radiation fluxes. The flux divergence/convergence is determined by taking the difference between upwelling and downwelling radiation. It is this difference that drives cloud top cooling, since upwelling IR is typically several tens to  $>100$  Watts/meter greater than downwelling IR (Wood 2012). This unstable configuration of cooling air aloft is the primary convective driving force within stratocumulus clouds. Indeed, Nicholls and Leighton (1985) concluded that radiative cooling driven from the cloud top was the primary source of convection and turbulent mixing within the cloud.

Although IR radiative forcing is of primary importance, the diurnal effects of shortwave solar radiation cannot be ignored. The net heating effect of solar radiation is typically much less than the heating/cooling rates associated with IR radiation. Cloud droplets are very effective at scattering most wavelengths of the visible spectrum, leaving only a few small near-infrared (NIR) wavelength bands available for absorption and associated heating of the cloud layer. For this reason, studies such as those of Slingo, 1989 have concluded that the absorbed percentage of solar radiation is typically less than 15 percent and more likely only a few percent.

*c. Turbulence*

Due to the convective nature of stratocumulus clouds, the vertical turbulent component of the wind greatly outweighs the importance of the mean wind, when considering turbulent fluxes. The vertical turbulent fluxes are the mechanism that transports and distributes heat and moisture throughout the STBL and hence maintains the vertical thermodynamic structure previously described.

Turbulent kinetic energy (TKE) is primarily generated by buoyancy flux within the stratocumulus cloud layer. Buoyancy flux near cloud top occurs due to the negative buoyancy resulting from radiation and entrainment processes. Buoyancy flux near the cloud base results from positive buoyancy due to IR radiative flux convergence and latent heat release. (Schubert et al. 1979a) These buoyancy fluxes generate turbulent up and down drafts that differ greatly in their temperature and water content. Dry air entrainment and radiational cooling processes at cloud top make the downdrafts cooler and dryer than adjacent updrafts, this leads to a vertical irregularity of the cloud base, as the LCL for up and downdrafts varies. For a layer to remain well mixed, the vertical energy and moisture fluxes must be linear functions of height (Wood 2012).

The shear generation term in the TKE equation is small throughout the mixed layer, except very close to the surface (Nicholls, 1983). An analysis of TKE balance shows that buoyancy production and dissipation are largest near the surface and just below cloud top (Nicholls, 1983). Specifically, Nicholls (1988) showed that in the upper part of the cloud layer, the buoyancy production term is large and positive while the transport and dissipation terms are negative. This indicates that the radiative cooling induced buoyancy term is dissipated by transport of downdrafts, and dissipated locally by molecular and eddy viscosity. Furthermore, Nicholls (1988) showed that the pressure redistribution term is large near cloud top, meaning that pressure redistribution of TKE is significant. This redistribution of TKE between vertical and horizontal components is consistent with the inversion constrained mesoscale convective updraft and downdraft flow fields described later.

Nicholls (1988) found that buoyancy flux is a maximum in the upper part of the STCU cloud, while decreased to small or negative values occur in the lower mixed layer. This finding confirmed the theory that cloud top radiative cooling was the primary process responsible for buoyancy production and convective motions. Nicholls also found that total water flux was a maximum near the cloud top.

Vertical variations in the horizontal wind components are typically small within the STBL, with larger values occurring at the cloud top / EIL interface, and near the surface. Due to the importance of buoyancy production in creating convection, the maximum vertical velocity variance occurs in the upper half of the cloud, and during late morning, where and when buoyancy production is maximized.

The surface latent heat flux (LHF) and sensible heat flux (SHF) are also important to stratocumulus dynamics. In the shallow and stable STBL typical of the California coast, these fluxes are small when compared to fluxes associated with type A cyclogenesis events and associated post frontal stratocumulus clouds. But nonetheless, the moisture and heat fluxes must be considered.

#### *d. Entrainment*

In the context of STBL dynamics, entrainment typically refers to the mixing of warmer and unsaturated air from the capping inversion into the top of the STBL. Entrainment is complicated by the presence of clouds at the entrainment interface. Entrainment at cloud-free inversions is more simplistic because it is primarily forced only by sheer-generated turbulence and the stability of the interface, which is a function of the vertical density gradient. However, Nicholls and Turton (1985) concluded that clouded interfaces are further complicated due to density fluctuations that can be caused by radiative and evaporative cooling. From aircraft transects flown 30 meters below the cloud top, Nicholls and Turton (1985) concluded that significant mixing is confined to an area a few tens of meters deep, and that vertical velocity fluctuations associated with downdrafts are not yet established. But at 50 meters below cloud top, downdrafts were observed to be organized features, and vertical velocity variance increased. From in-situ aircraft measurements, Nicholls (1988) found that entrained air accounted for only .7 to

three percent of the air within downdrafts, noting that despite a small contribution from evaporative cooling, the warmer entrained air had a net positive buoyancy effect, confirming that radiative cooling was the primary physical mechanism causing downdrafts.

The entrainment rate ( $w_e$ ) at the cloud-top/ EIL interface is the primary variable quantifying entrainment, and is still poorly understood. Deardorff (1980a) concluded that  $w_e$  is equal to the sum of turbulent entrainment and non-turbulent STBL deepening, with turbulent entrainment primarily governed by turbulence production, leading to a positive feedback mechanism. The buoyancy production resulting from radiative cooling can lead to further negative buoyancy via a process known as buoyancy reversal. As described by Wood (2012), this occurs when the negative buoyancy resulting from evaporative cooling outweighs the positive buoyancy resulting from the warmer and less dense entrained air. This net negative buoyancy effect can enhance the downdraft and associated entrainment. This process is called cloud-top entrainment instability (CTEI). CTEI can lead to a positive feedback cycle that acts to dry the STBL and breakup the cloud layer.

*e. Drizzle/Precipitation*

Although it is not a dominant factor in effecting STBL dynamics, the effect of drizzle should be understood. Pincus et al, 1997, noted that precipitation influence on STBL dynamics are twofold; first, the downward distribution of liquid water through the STBL and second+, the thermodynamic effects from the moistening and cooling of the sub-cloud layer resulting from evaporation. The net effect of drizzle is to stabilize the STBL via latent heating and cooling within the cloud and sub-cloud layers, respectively. These thermodynamic effects are typically small compared to the radiative forcing, and confined to areas of significant drizzle. Leon et al. (2008) noted that persistent marine stratocumulus areas, such as the California coast, experience light drizzle only 20 to 40 percent of the time. Multiple studies, including those by Bretherton et al. (2004), have shown that drizzle is at a maximum during the early morning. This is due to the daily radiative forcing cycle and the associated increases in convection and liquid water

content. Using lagrangian-based observing techniques, Pincus et al. (1997) concluded that in shallow boundary layers typical of the California coast, precipitation is not a primary factor in determining cloud fraction.

## **2. Mesoscale Processes**

When the effects of the previously described macro-scale physical processes are considered over larger cloud surface areas, their net effect is to self-organize into larger convective motion fields. As noted by Wood (2012), the wide spectrum of possible interactions between all of the previously described microphysical and macro-physical processes is ultimately the reason behind the wide variety of morphological forms exhibited by stratocumulus clouds. For this reason, an understanding of the primary positive feedback processes responsible for the horizontally homogenous nature of stratocumulus clouds is required, as deviations from these processes contributes to mesoscale variability. The foremost positive feedback process was coined the cloud-radiation-turbulent-entrainment feedback by Zhu et al. (2005). This is a process of stratocumulus self-regulation in which thickening clouds experience larger amounts of buoyancy flux and evaporative cooling by virtue of their vertical thermodynamic structure, which in turn leads to increased turbulence and associated entrainment, which acts to reduce thickness. Conversely, thinning clouds experience reduced entrainment, which promotes thickening. Additionally, precipitation can have a strong regulating effect on stratocumulus thickness because the increased stability (and associated reduced turbulence and associated entrainment), acts to reduce moisture loss of STBL, making up for the moisture loss from precipitation.

Since precipitation is strongly dependent on cloud microphysical properties, cloud microphysics play an important role in these feedback mechanisms. In general, larger amounts of  $N_d$  result in reduced precipitation because more, smaller droplets inhibit the coalescence and autoconversion process (Wood 2012).  $N_d$  can also affect turbulence within the STBL. Wang et al. 2003 found that the increased droplet surface area associated with higher  $N_d$  can result in an increased rate of condensation and evaporation, thereby increasing associated latent heating and cooling rates and associated buoyancy

generated TKE. Due to thickness limiting physical feedback mechanisms, Wood (2012) noted that Stratocumulus thickness ( $h$ ) exhibits a lack of variability, typically ranging from 200 to 400 meters.

### **3. Synoptic Scale Processes**

Over periods in excess of several hours, advective effects controlled by the synoptic-scale flow will exert an important influence on cloud structure. Most notably, stratocumulus clouds are affected by synoptic atmospheric parameters such as divergence, free tropospheric moisture and temperature, and lower-tropospheric stability (LTS). Atmospheric divergence and cloud top entrainment rate act to oppose each other and determine the depth of the boundary layer. Therefore, divergence plays an indirect role in determining STBL dynamic and thermodynamic structure and processes. The exact role that free-tropospheric moisture content plays in STBL dynamics is still unknown. Several processes act to simultaneously increase and decrease stratocumulus thickness. Wood (2012) summarized that the entrainment of dryer air tends to raise the LCL of convective downdrafts, which would tend to decrease cloud thickness, but also, the dryer air results in increased evaporative cooling, which would tend to increase downdraft negative buoyancy and enhance associated mixing and entrainment, thereby raising the cloud top level. The exact interplay between these two processes is still not fully understood.

Klein and Hartmann (1993) noted that higher LTS, which is typically determined by the difference between the 1000 hPa and 850 hPa potential temperatures, can be directly correlated with higher spatial coverage of stratocumulus clouds. The increased LTS results in a stronger cloud-top inversion and associated reduced rates of entrainment, which in-turn forces a shallower, more horizontally extensive stratocumulus layer (Wood and Bretherton 2004).

The strong presence of stratocumulus within the Eastern portions of subtropical ocean basins is largely controlled by synoptic and global scale atmospheric and oceanic flows. Wood (2012) noted that stratocumulus clouds preferentially form over the cold (eastern) parts of ocean basins due the increased lower-tropospheric stability resulting

from synoptic scale flow over a cold ocean surface. This region of the ocean also coincides with low and strong subsidence inversions due to subsiding air within the downward branches of global scale atmospheric motions such as Hadley cells.

Pincus et al. (1997) used lagrangian techniques to conclude that large scale changes in sea surface temperature (SST) and atmospheric parameters have been shown to significantly affect stratocumulus evolution on time scales of a few days. Specifically, he found that over short time scales, rapid increases in SST are associated with thicker clouds and a higher cloud fraction due to increased fluxes of heat and moisture from the sea surface into the boundary layer (Pincus et al. 1997). However, over longer time scales, a consistently warmer SST was found to increase the depth of the boundary layer and eventually led to reduced cloud fraction.

Synoptic variations in sea surface temperature also play a crucial role in stratocumulus formation and sustainment. Prior to stratocumulus formation (and associated radiative and evaporative sources of turbulence), positive buoyancy generated at the ocean surface is the primary source of TKE, and can lead to saturation and vertical mixing within the PBL, which can initially form stratocumulus clouds, although this formation process is still poorly understood. A combination of the surface affected parcels' temperature and moisture perturbations from the mean characteristics of the surface layer determines the buoyancy of the parcel. Wood (2012) noted that since the moisture perturbation is typically always positive due to surface evaporation, it is the temperature perturbation that ultimately determines the buoyancy of parcels in contact with the ocean surface. The temperature perturbation depends on the temperature difference between the sea surface and the overlying air.

On global scales, the areas of persistent stratocumulus cover are confined to eastern subtropical ocean basins. In these regions, the annual mean of stratocumulus cover exceeds 40 percent and can be as high as 60 percent (Wood 2012). These areas contain large-scale atmospheric conditions that are ideal for stratocumulus formation and sustainment. Most notably, a stable lower-stratosphere and a strong and low temperature inversion are ideal conditions. These mean atmospheric conditions are the result of persistent global scale atmospheric and oceanographic motions.

On synoptic scales, the areas of persistent stratocumulus cover are associated with synoptic high pressure systems. More specifically, cold-air advection and large-scale subsidence on the eastern side of subtropical ridges provides an environment suitable for stratocumulus development (Norris and Klein 2000). For this reason, synoptic variability of stratocumulus clouds can be directly correlated with the variability of synoptic weather features, which should therefore be taken into account when analyzing the temporal evolution of stratocumulus regions.

### C. STRATOCUMULUS MESOSCALE VARIABILITY

A clearly defined pattern of mesoscale convective cellular structure is the most typical form of mesoscale variability. This structure can be further sub-divided into four mesoscale morphological types as shown in Figure 2: no cellularity on the mesoscale, organized closed mesoscale cellular convection, organized open mesoscale cellular convection, and unorganized mesoscale cells (Wood 2012).

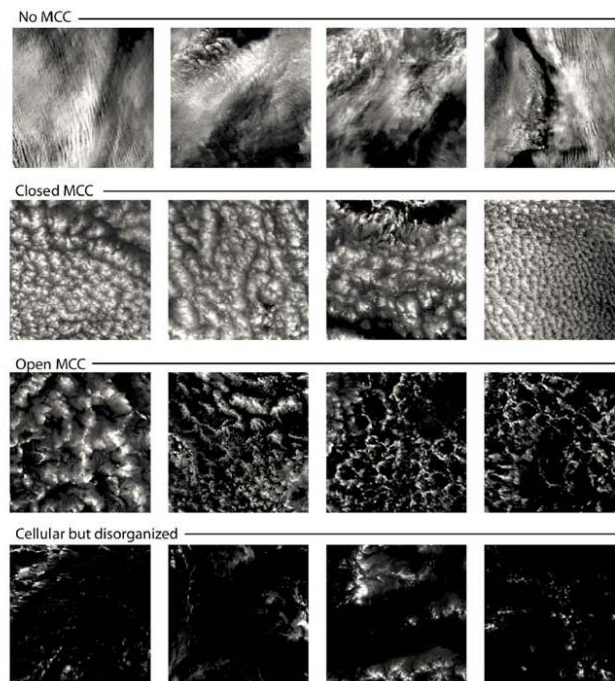


Figure 2. Various forms of MCC (from Wood 2012).

Stratocumulus clouds can also be organized into linear row structures also known as horizontal roll vortices. These structures form in areas with marked wind shear across the STBL (Atkinson and Zhang 1996). Aside from short lived instances following cold front passage, their primary spatial distribution is limited to the area north of the equatorial pacific cold tongue (Wood 2012).

### **1. Temporal Variability**

Stratocumulus clouds vary over a large range of timescales, in response to a variety of forcing. Although temporal variability is not the central focus of this thesis, a basic understanding of the time-varying dynamic forcing and resulting cloud response is a useful background in conceptualizing mesoscale dynamics.

Over long time scales, stratocumulus variability can be linked to processes that act to alter lower tropospheric stability. Most notably, lower tropospheric stability is strongly connected to the sea surface temperature (Hanson 1991). For this reason, cyclical phenomena such as El Nino and the Southern Oscillation can alter stratocumulus variability indirectly through large scale SST variations. The seasonal variation of lower-tropospheric stability (LTS) results in a corresponding seasonal cycle of stratocumulus clouds. For this reason, the semi-permanent subtropical marine stratocumulus sheet of the eastern Pacific reaches its maximum extent in the northern hemisphere summer.

Although stratocumulus clouds do have slight variability over long timescales in response to large-scale atmospheric motions, more significant variation occur with the diurnal cycle. Stratocumulus properties undergo considerable changes on hourly to daily time-scales that are driven by the diurnal cycle of incoming solar radiation (Pincus et al. 1997). The net effect of daytime solar radiation is to offset some of the radiative cooling occurring at cloud top, and effectively dampen the convective forcing of the stratocumulus cloud. For this reason, stratocumulus clouds tend to have their maximum coverage in the early morning (Wood 2012). This strong response to the daily cycle of shortwave radiation is a testament to the importance of radiative forcing in stratocumulus dynamics.

## 2. Mesoscale Cellular Convection

Mid-latitude mesoscale cellular convection (MCC) in the western ocean basins is most often observed when extra tropical lows move over western boundary currents. The large temperature difference between the cold polar air mass and the warm current results in large heat and moisture fluxes. These fluxes aid the formation of open cell convection. MCC in the eastern ocean basins is typically associated with marine stratocumulus, and the radiative and evaporative processes previously described. The resulting spatial distribution of typical areas of frequent MCC is shown in Figure 3.

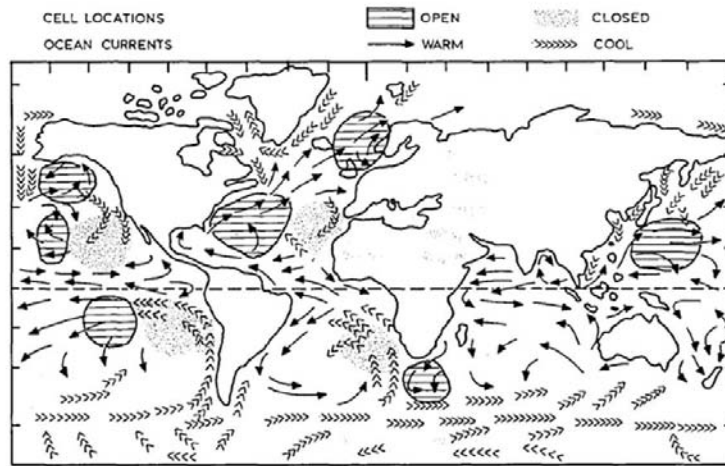


Figure 3. Spatial extent of MCC (from Agee 1987).

Due to the stronger forcing, and the convection being forced from below, western ocean basin MCC more closely resembles the classical and idealized Bernard-Rayleigh convection (Agee 1987). However, marine stratocumulus MCC is an analogous convection process, in the inverted sense. The only difference is that the primary source of convective forcing is cooling aloft, rather than heating from below. Regardless of the forcing, the resulting convective circulations typically organize into quazi-hexagonal cells, with a wide range of physical dimensions. Due to the low and strong capping inversion, the horizontal scale of the cells is much larger than the vertical scale, resulting

in large aspect ratios. Cell diameters vary across the meso-gamma and meso-beta spatial scales, most typically within the 10–100 km range (Agee 1987).

The horizontal length scale of MCC exhibits significant temporal variability. Convective onset is characterized by smaller horizontal scales, known as a basic convective mode (BCM), which subsequently transitions to a MCC mode with larger horizontal scales (Agee 1987) as it is forced by physical processes previously described. This cascading of energy from higher to lower frequencies is best analyzed via spectral analysis.

### **3. Previous MCC Research**

The first generation of television infrared observation satellites (TIROS) made it possible to advance convective theory from the laboratory to the atmosphere. Krueger and Fritz, 1961 utilized TIROS imagery to observe MCC over the oceans. They noted that the organized hexagonal structure greatly resembled that of classical Bernard-Rayleigh convection. Later satellite analysis by Hubert (1966) showed that MCC exhibited smaller, turbulent scales of motion that were imbedded within the larger scale circulations.

Driven by a need for better spatial and temporal resolution data and advances in aircraft instrumentation, the 1970s saw advances in the in-situ examination of MCC and associated dynamic and thermodynamic structure. The Air Mass Transformation Experiment (AMTEX) conducted in 1975 utilized data collected from an NCAR Electra research aircraft and defense meteorological satellite program (DMSP) satellite imagery to analyze closed-cell stratocumulus convection over the Western Pacific. In their analysis of the data set from the experiment, Rothermel and Agee (1979) focused on the horizontal transects of two closed cells. Their results confirmed the upward motion of warm, moist air within the cell centers, impinging upon the overlying inversion and horizontally diverging /cooling to form organized downward motions of dryer air in cell walls (Rothermel and Agee 1979). Their study contributed greatly to the knowledge of macroscale processes occurring within stratocumulus clouds, and contributed to a conceptual model of MCC dynamics.

The conceptual understanding of closed cell MCC was advanced further during the marine stratocumulus phase of the first ISCCP (International satellite cloud climatology project) regional experiment (FIRE). During their analysis of the data set from derived from this experiment, Moyer and Young (1994) averaged the mesoscale variations in kinematic and thermodynamic properties obtained during 45 aircraft transects through MCC.

#### **D. UPPEF MEASUREMENTS OVERVIEW**

UPPEF 2012 consisted of 12 flights utilizing the Twin Otter research aircraft operated by the Center for Interdisciplinary Remote-Piloted Aircraft Studies (CIRPAS). These research flights collected data throughout the extensive marine stratocumulus layer west of Monterey, California during September, 2012. UPPEF 2012 was sponsored by the Office of Naval Research with an ultimate goal of improving cloud parameterizations in forecasting models by investigating the dynamic and thermodynamic processes occurring within the STBL. Of the 12 research flights (RF), four (RF05, RF06, RF08, and RF10) exhibited significant cellular mesoscale variability within the STBL. In particular, RF05 and RF10 had extensive regions of open and closed mesoscale cellular convection that were transected by the aircraft. For this reason, RF05 and RF10 will be examined in depth. For a detailed overview of all UPPEF2012 flights, including a flight and instrumentation summary, see Tellado (2013).

##### **1. Synoptic Summary for RF05 and RF10**

A brief summary of synoptic conditions is presented here to provide a general context to the large scale dynamics influencing the STBL region of interest during RF05 and RF10. Reanalysis products from the National Centers for Environmental Prediction / National Center for Atmospheric Research (NCEP/NCAR) Earth System Research laboratory (ESRL) physical sciences division are shown in Figures 4 and 5 to summarize synoptic conditions.

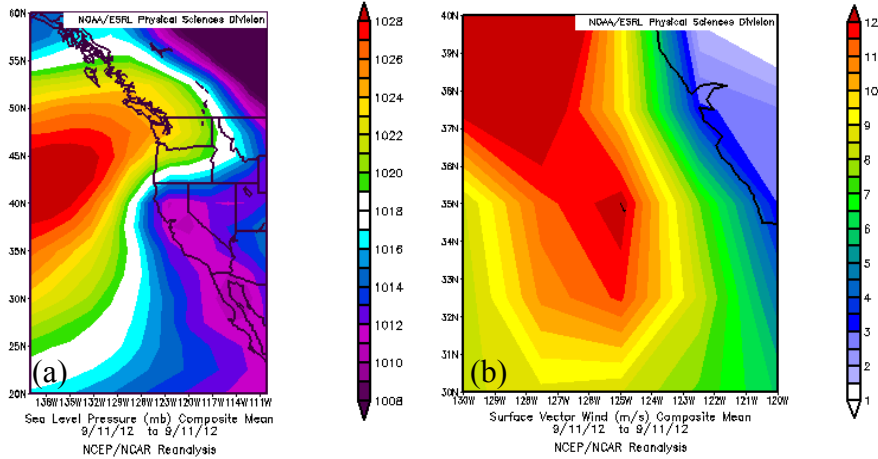


Figure 4. (a) Sea level pressure and (b) surface vector winds during RF05.

RF05 was conducted on the morning of September 11, 2012. At this time, the Eastern Pacific (EPAC) high has built to 1030 mb and ridged to the NNW. Sustained regional high pressure has enhanced surface heating over the desert south west and North through the central valley, resulting in a thermal trough. The orientation and proximity of these high and low pressure regions results in an enhanced zonal pressure gradient with associated enhanced northwesterly winds over the STBL region of interest

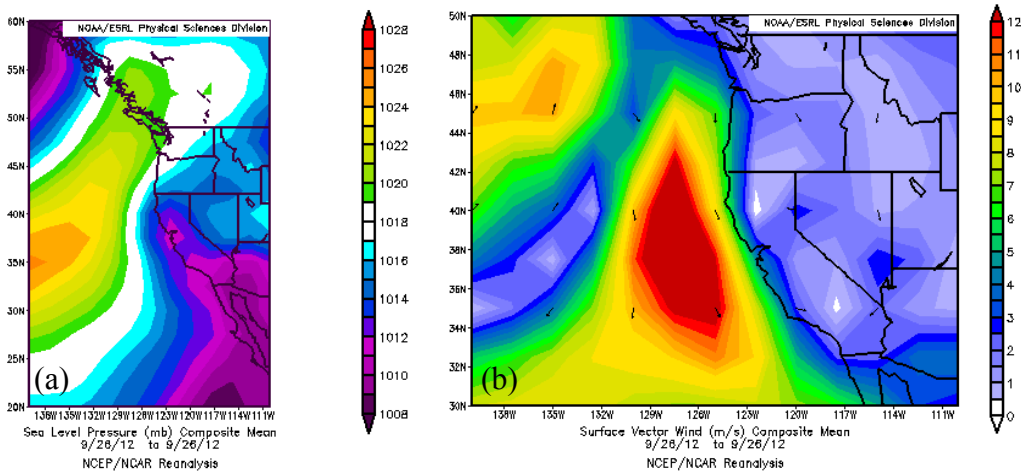


Figure 5. (a) Sea level pressure and (b) surface vector winds during RF10.

RF10 took place on September 26, 2012. The EPAC high has weakened and moved south from its' typical position. The thermal trough over the West Coast has also slightly weakened due to reduced surface heating. The resulting reduced pressure gradient is inducing northwesterly winds over the STBL region of interest.

### **III. ANALYSIS OF SATELLITE OBSERVED CLOUD STRUCTURE**

#### **A. UPPEF2012 CLOUD STRUCTURE OVERVIEW**

With 12 flights totaling nearly 50 hours of data collection through a variety of stratocumulus mesoscale features, it was clear from the onset that a qualitative analysis of satellite imagery would be needed to identify the flights that transected mesoscale features of interest. To do this, the visible bands of the Moderate-Resolution Imaging Spectroradiometer (MODIS) instrument were examined. These images were collected from the morning, descending-pass of the polar, sun-synchronous orbiting Terra satellite vehicle. Shown in Figure 6, these images display the mesoscale characteristics of the stratocumulus layer occurring during the morning hours (approximately 2100 GMT) that roughly correspond to the time of the research flights. Since advection and evolution of cloud features has not been taken into account, these images closely, but not exactly, corresponds with the actual features the aircraft transected due to the small time offset between aircraft and satellite data collection times. Nonetheless, this method serves as an adequate initial method of identifying features of interest.

The spatial variability of cloud structure during the morning of each UPPEF flight day is shown in Figure 6. The imagery corresponding to flight RF01 shows a narrow coastal swath of closed and disorganized cellular structure parallel to the coast and a clear rift zone further offshore. During flight RF02, the STBL was organized into closed MCC throughout the entire region. There is some indication of the cells being organized into row structures parallel to the coast, especially further offshore. Flight RF03 was conducted through a nearshore clearing, which transitions to open and disorganized cellular structure further offshore. The imagery corresponding to flight RF04 indicates clear nearshore conditions that transition to a non-cellular STBL offshore. During RF05, the STBL was organized into closed MCC with significant row structures becoming more identifiable further offshore. Flight RF06 was conducted through a region of nearshore closed MCC with a clear rift zone further offshore and larger diameter MCC even further offshore. During flight RF07, the STBL was largely horizontally homogenous with

indications of imbedded large diameter closed MCC. Flight RF08 transected a narrow swath of varying diameter, closed MCC. The imagery corresponding to flight RF09 shows disorganized cellular structures offshore and clear conditions nearshore. During RF10, the STBL was organized into an extensive layer of closed MCC, which gradually transition to open MCC further offshore. RF11 and RF12 were flown in clear conditions.

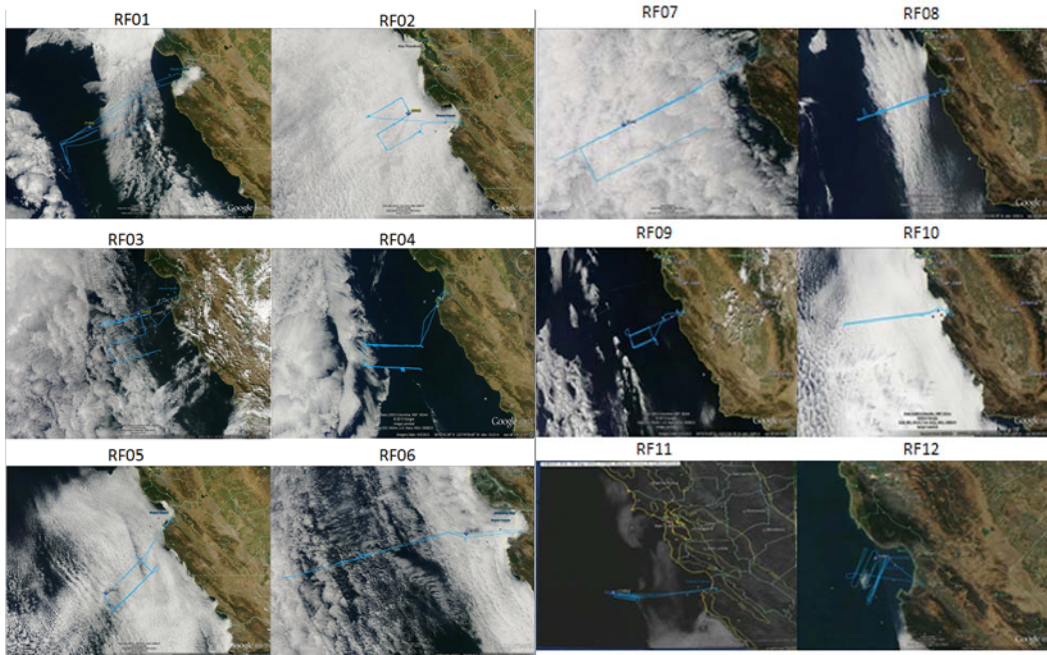


Figure 6. Cloud structure variability during UPPEF 2012. Blue lines indicate approximate flight tracks (from Tellado 1013).

## B. ANALYSIS OF CLOUD STRUCTURE FROM GOES IRRADIANCE MEASUREMENTS

Although MODIS imagery was utilized for the initial qualitative assessment, with only one morning satellite pass over our region of interest, it lacks sufficient temporal resolution. Increased temporal resolution allows for a better analysis of the variations to STBL mesoscale structures throughout the morning hours, and a better correlation between aircraft and satellite data due to a decreased data valid time offset. For these reasons, data from the Geostationary Operational Environmental Satellite (GOES) will be used for further analysis. With continuous coverage of the Western United States, GOES-15 provides data at 15 minute intervals, rather than once per morning with MODIS.

## **1. Analysis Methodology**

In order to undertake a quantitative analysis of GOES data, raw data from the National Oceanic and Atmospheric Administration's (NOAA) comprehensive large array-data stewardship system (CLASS) website was utilized. Although GOES collects data in five distinct spectral bands, only the visible band was utilized. Denoted as "Band 1," the visible band collects upwelling reflected solar irradiance in the .55 to .75  $\mu\text{m}$  spectral ranges. By making a few assumptions, the irradiance values obtained from band 1 can be attributed to STCU albedo.

In order to attribute visible irradiance variations solely to STCU albedo variations, the underlying ocean surface albedo must be negligible and horizontally homogenous over the area of interest. Although this assumption cannot be confirmed, because satellite derived ocean color products are not generated over areas obscured by cloud cover, this is generally a valid assumption in open ocean applications, where visible reflectance very small and not significantly altered by biologics and sediments.

We must also confirm that upper level cirrus clouds are not superimposed over the STCU area of interest. Significant cirrus cover would increase irradiance values collected by GOES band 1, and lead us to falsely attribute this increase to an increased STCU albedo. A quick assessment of the MODIS derived cirrus reflectance product downloaded from NASA's Land and Atmosphere Archive and Distribution System (LAADS) and shown in Figures 7 and 8 confirms that negligible cirrus presence existed during the time and location of interest.

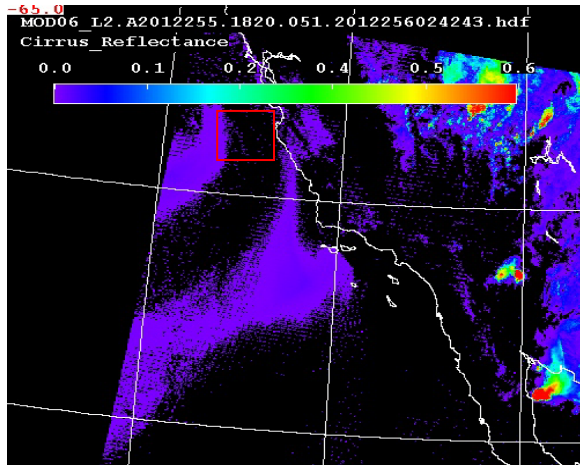


Figure 7. Cirrus cloud reflectance during RF05

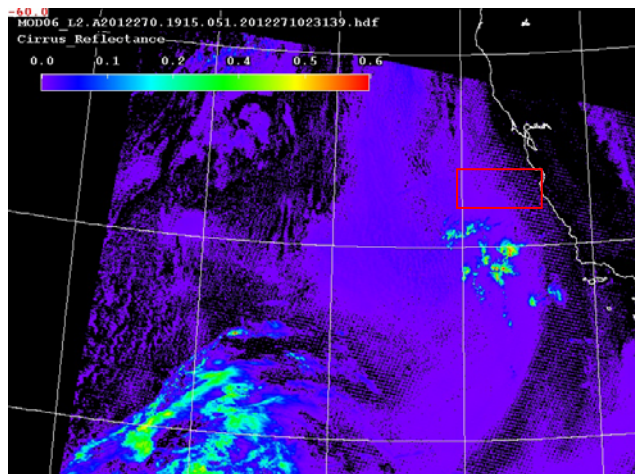


Figure 8. Cirrus cloud reflectance during RF10

Now that the STCU albedo has been confirmed to be the primary contributor to the GOES-collected irradiance, the albedo can be related to other properties of the STBL. Liou (1992) concluded that albedo is a function of four parameters: optical thickness, the single-scattering albedo, the asymmetry parameter, and the solar zenith angle. Since GOES band 1 collects irradiance solely in the visible portion of the spectrum, the single-scattering albedo and the asymmetry parameter can be assumed to be constants. Since our analysis will compare irradiances collected from a single satellite valid time over a small spatial area, the solar zenith angle can be considered a constant as well. Therefore, the GOES-collected irradiance values can be directly correlated to the cloud optical

thickness. Since, the cloud optical thickness is a strong function of the LWP of the cloud layer (Wood 2012) we can use our GOES-collected irradiance values as a proxy for LWP, and expect to see good agreement with in situ measured liquid water measurements.

The primary disadvantage of using GOES measurements is the coarse spatial resolution compared to the 250 meter resolution of MODIS measurements. The spatial resolution of GOES band 1 is stated as one km at nadir. However, the geometry between the satellite position over the equator and the area of the Earth being scanned makes the resolution a function of both latitude and longitude. This results in a nominal decrease in spatial resolution to approximately 1.2–1.3 km due to the slanted viewing angle of the satellite. However, this disadvantage is negated by the increased temporal resolution of GOES. Because the MCC structures of interest to this study are on the scale of tens of km, the GOES measurements can still provide adequate resolution to resolve these features. Under “routine” scan mode operations, GOES does a full-disk scan of the entire northern hemisphere over a 7–15 minute time window. Also imbedded within its scan schedule is a rapid scan operation (RSO) mode, in which it scans the sub-continental U.S over a 3–5 minute time window. GOES data with a valid time closest to the research flight time was selected for analysis.

Raw data was downloaded from CLASS in network common data form (NetCDF) file format, and imported into MATLAB for analysis. Data was downloaded in 16 bit format and converted to 10 bit by dividing by 32. This yields data in units of un-calibrated irradiance. To account for post-launch instrument drift inaccuracies, these values were then calibrated by utilizing the GOES-15 calibration instructions from NOAA’s Center for Satellite Applications and Research (STAR). A correction factor of 1.265 was applied to the data values.

The calibrated irradiance was quantitatively analyzed in the MATLAB environment. Figures 9 and 10 show a plan-view depiction of the cloud field observed during RF05 and RF10. The original GOES imagery in .jpg format is also shown for reference. Since these images are produced from the same data set, they should look

identical, with lighter colors on the grey scale corresponding to warmer colors on the MATLAB generated image. The consistency between the two images confirms the validity of our satellite data processing techniques.

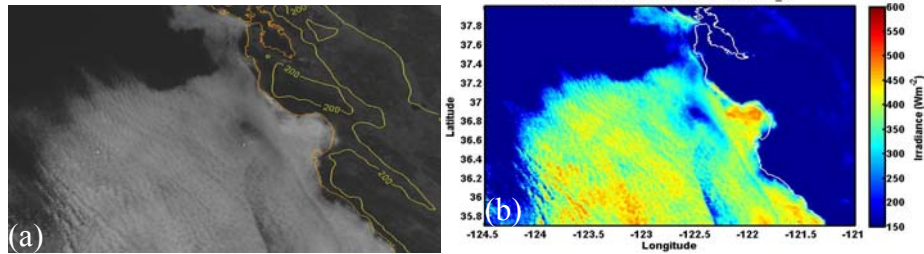


Figure 9. Cloud field from RF05. (a) GOES image and (b) MATLAB generated from GOES data.

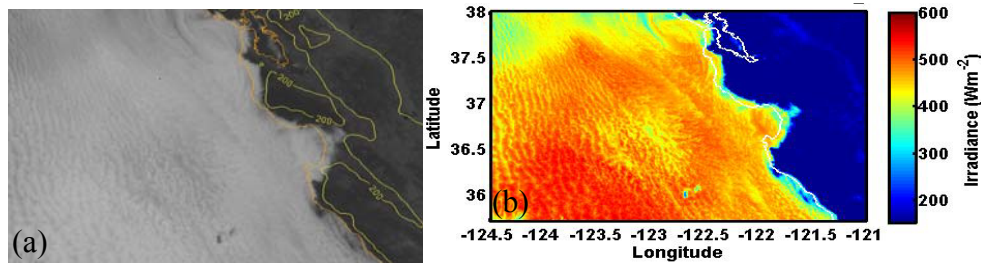


Figure 10. Same as in Figure 9, except for RF10.

In order to determine the dominant spatial scales of variation for MCC that are comparable to aircraft measurements, irradiance measurements from a linear transect must be extracted from the original data. To do this, MATLAB's "triscatteredinterp" function was used to linearly interpolate the data set into a regularly spaced grid of data values. Then, a string of coordinates defining our linear cross section location was created and sampled the interpolated data set at a constant sampling distance of .5 km along the transect line. Figure 11 shows the variation of irradiance as a function of distance along the transect, with the data extracted from the original 2-D irradiance.

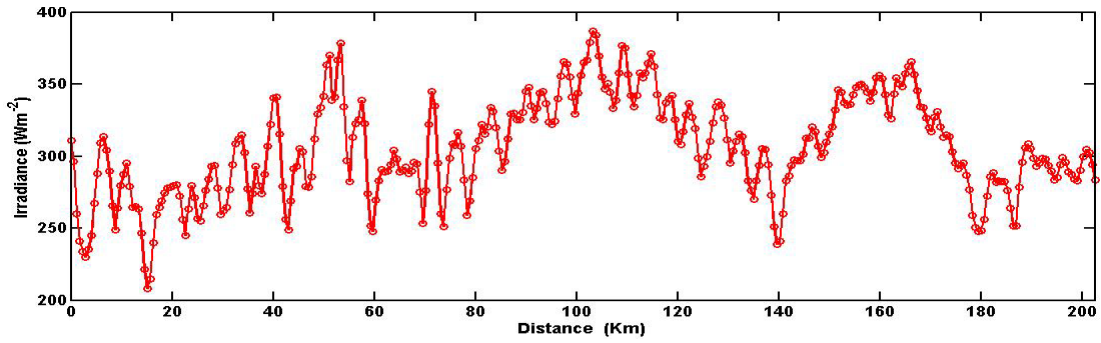


Figure 11. Sample GOES Radiance cross section from RF05 closed cell MCC.

A quick glance at this irradiance cross section shows that large variations in irradiance are observed across the cloud top. Several scales of variation exist in this data segment. Low frequency variations in the irradiance (such as the increase in irradiance from 80 to 140 km in Figure 11) generally correspond with a broad area of thicker cloud. In order to isolate mesoscale perturbations in the irradiance, a third order Butterworth filter was used to remove length scales greater than 40 km. The remaining high frequency/small scale variations in irradiance correspond with smaller scale changes in LWP associated with the updraft and downdraft regions of the MCC.

Sampling large features that exist over a limited spatial area poses challenges to obtaining statistical significance. To overcome this, multiple parallel cross sections were taken to increase the number of samples in the features of interest. As shown in Figure 12, the cross sections were taken through regions of relatively uniform cloud scale characteristics in order to accurately reflect area statistics. The transects were also separated adequately as to not sample the same MCC features as adjacent transects. Since the linear rows of MCC often align parallel with the synoptic scale wind, transects were drawn perpendicular to the mean with in order to intersect the linear features at right angles.

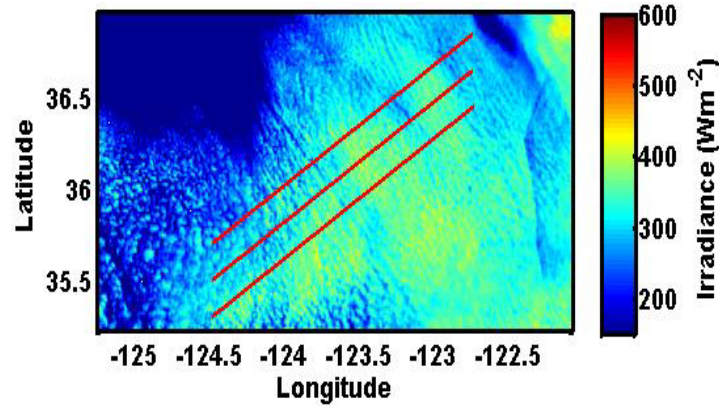


Figure 12. Illustration of 1-D sampling from the 2-D irradiance field of satellite measurements.

Figure 11 shows that the irradiance cross section has sinusoidal variations that seem to exist at discrete frequencies, suggesting a dominant scale of variation. A spectral analysis of the irradiance cross sections was undertaken to identify the specific frequency components, and hence dominant spatial scales of variation within the STBL. To do this, the power spectral density (PSD) was calculated using MATLAB’s “psd” function and averaged in the frequency domain. As shown in Figure 13, the smoothed PSD was calculated independently for each of the parallel transects, and then averaged among multiple transects to yield “area-averaged” spatial statistics. This methodology results in more statistically significant irradiance spectra.

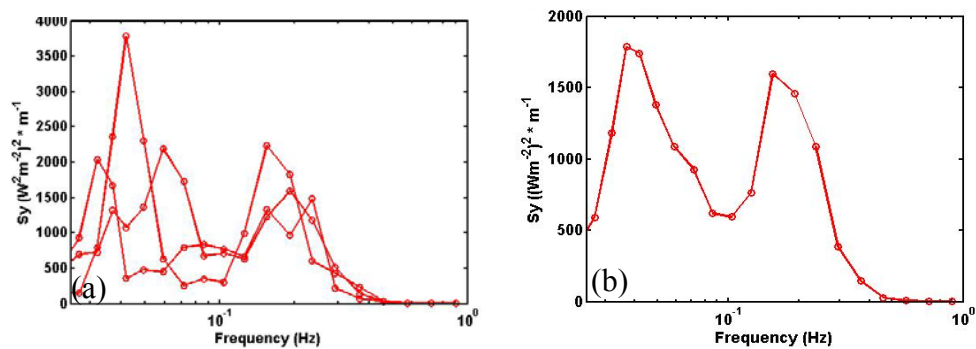


Figure 13. Multiple transect averaging process. (a) PSD from individual transects and (b) “area-averaged” PSD from three transects in (a).

As shown in Figure 13, the averaging process smooths the spectral peaks that exist at slightly differing frequencies and magnitudes within each individual transect. Also note that the PDS from each individual transect resembles the averaged PSD. This is a good indication that our three transects exist in an area of relatively homogeneous spectral statistics. Using this methodology, the spatial variability of the cloud field can be analyzed.

## 2. Spatial Variability

### a. RF05

During this research flight, the STBL transitions from nearshore closed cell MCC to offshore open cell MCC. The spectral characteristics of these two distinct regions are the emphasis of this section. As shown in Figure 14, the nearshore transects correspond with the closed cell MCC region in which the research flight was conducted. The valid time for this GOES image is 1800 GMT, which corresponds with the Twin Otter flight time. Further offshore, open cell MCC becomes prominent, and synoptic winds veer slightly, hence the adjustment to the offshore transect orientation.

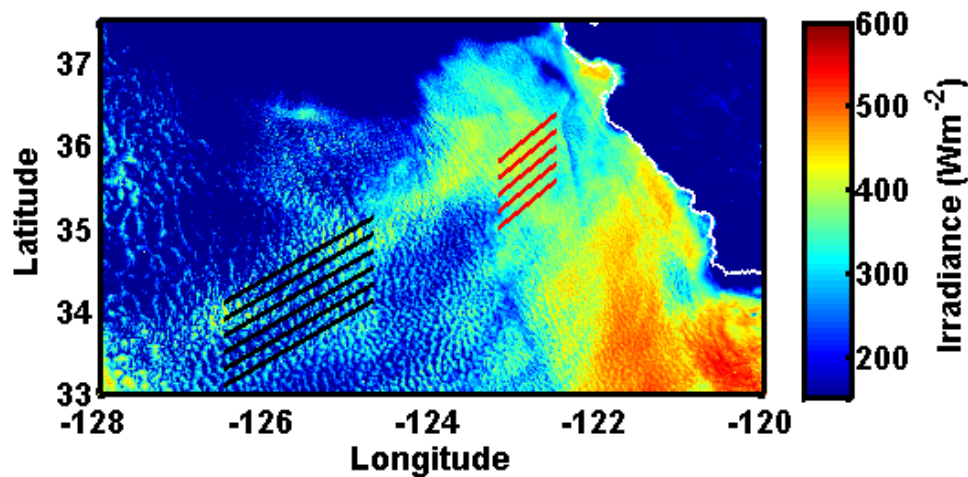


Figure 14. Nearshore and offshore cross section locations at 1800 GMT.

As shown in Figure 15 (a), the PSD calculated from the individual transects match well within each region, this is a verification of the spectral uniformity within each

region. The area averaged PSD calculated from these transects, shown in Figure 15 (b), indicate an offshore peak of .087 Hz and a broad peak between .105 Hz and .182 Hz in the nearshore region. The PSD for the two regions have the same general shape, which means the relative magnitudes of spectral components within each region are similar; however, the PSD of the offshore region is two orders of magnitude larger than the nearshore region across the .03 to .20 Hz frequency range and one order of magnitude larger across the remaining frequencies. Note that with a log y-axis, the spectral peaks appear less prominent than when plotted on a linear y axis. This difference in magnitude suggests large LWP variability in the offshore region, which is more likely to be visually considered as a broken cloud regime.

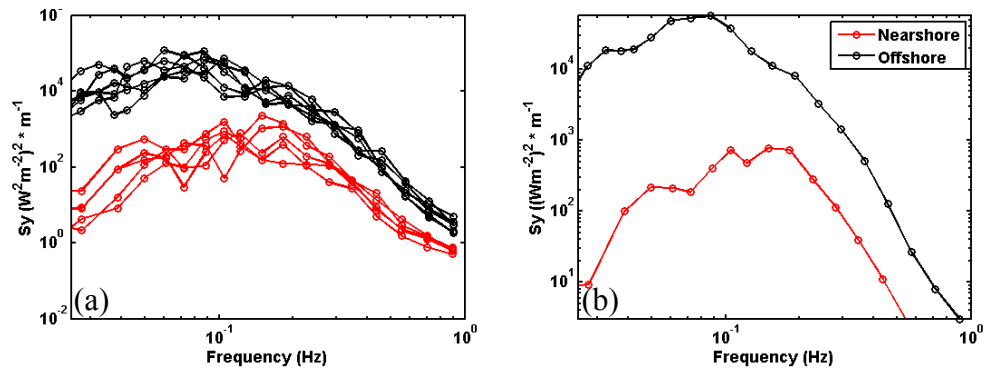


Figure 15. Log-log plots of nearshore (red) and offshore (black) (a) individual cross section PSD and (b) area-averaged PSD.

As shown in Figure 16, when the PSD is plotted as a function of wavelength, an offshore peak exists at 11.5 km, and nearshore peaks occur at 7 km and 9.5 km. The wavelength conceptually corresponds to the distance from cell center to adjacent cell center, and can be considered the preferred length scale for MCC. From these results, we can conclude that the larger irradiance difference between the clouded open cell center and cloud free area between open cells results in larger spectral components across all frequencies, particularly in the frequencies of maximum PSD. In this specific case, the wavelength of the offshore open cell region is slightly larger than that of the nearshore closed cell region.

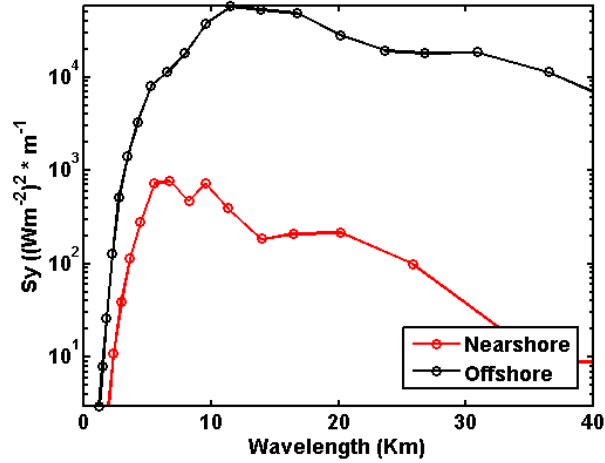


Figure 16. PSD of irradiance for nearshore and offshore region as a function of wavelength.

***b. RF10***

The spatial variations of the cloud fields during RF10 are similar to RF05. The linear out-and-back flight path was conducted entirely within the nearshore closed cell MCC region of the STBL, and corresponds with the red, nearshore transects. As shown in Figure 17, the nearshore closed cell STBL transitions to open cells further offshore over a relatively small distance. Note that the cross section locations have been chosen to avoid contamination from upper level clouds.

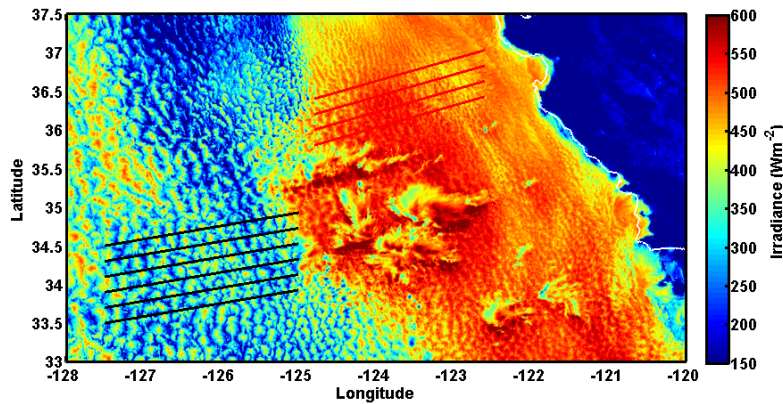


Figure 17. Nearshore and offshore transect locations for RF10.

Figure 18 shows the area averaged PSD calculated from the nearshore and offshore regions, which indicates an offshore peak of .051 Hz and a nearshore peak of .124 Hz. This frequency difference is much greater than that of RF05, suggesting a significant scale change with increasing offshore distance. Additionally, the offshore peak appears to be more prominent than in RF05, with the majority of energy existing in a narrower bandwidth of frequencies, this suggests a strong preference for MCC spatial scale of organization. Similar to RF05, the PSD of the offshore region is between one and two orders of magnitude larger than the nearshore region across all frequencies.

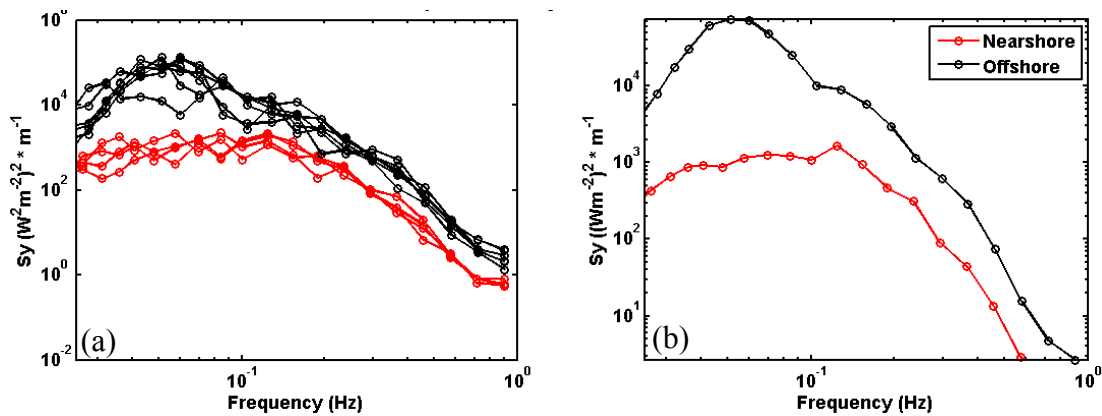


Figure 18. Log-log plots of nearshore (red) and offshore (black) (a) individual cross section PSD and (b) area-averaged PSD.

These frequencies correspond to wavelengths of 20 km for the offshore region and 8.5 km for the nearshore region, as shown in Figure 19. This result contrasts RF05, where only a very small scale increase was noted. Notably, the wavelength of the nearshore closed cell region is very similar between the two flights, suggesting a preferred length scale of cellular organization within nearshore closed cell MCC. These results will be related to the dynamic forcing existing within the STBL, as determined by the aircraft data analyses section of this thesis.

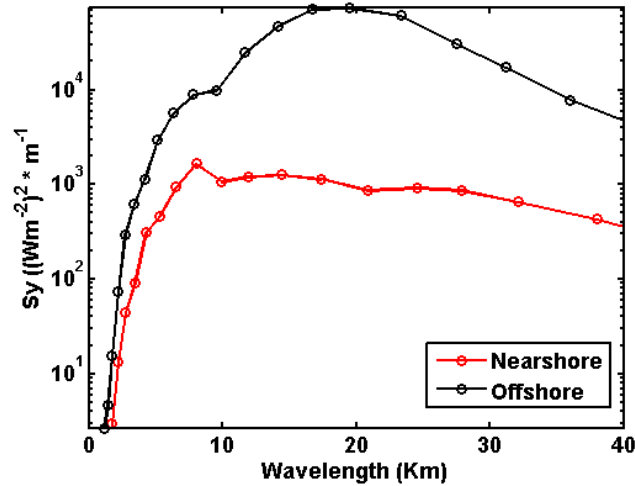


Figure 19. Same as in Figure 16, except for RF10.

### 3. Temporal Variability

#### a. RF05

The spatial variability analysis of the previous section was done at a valid time that corresponds to the aircraft measurement time. In order to assess the changes to the STCU throughout the morning hours, calculations and transect locations that were identical to the previous section were done two hours before and after the research flight time. As shown in Figure 20, the most notable difference is the increased irradiance later in the morning. This increase is due to the strong dependence of cloud albedo on the solar zenith angle. As the solar zenith angle increases when the sun rises, the cloud albedo and hence irradiance also increases. This increasing cloud albedo is the reason for the order of magnitude increase in spectral components throughout the morning. For this reason, the magnitude of calculated PSD components cannot be compared at different satellite valid times, but the frequency dependent magnitudes can still be compared within each valid time, allowing for the spatial scales of variation to still be determined.

Another notable point is that the STCU remains largely unchanged through the morning hours despite the radiative forcing applied by the rising sun. The spatial distribution of the STCU and the open cell and closed cell MCC regions remain in the same location throughout the morning.

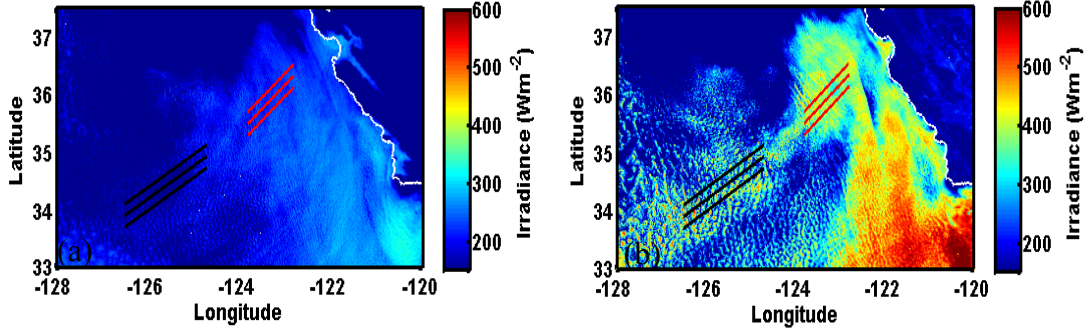


Figure 20. GOES irradiance (a) two hours prior and (b) two hours after RF05.

As shown in Figure 21, the area averaged PSD for the offshore region remains basically unchanged throughout the morning hours, with a PSD peak at a wavelength of around 12 km. This speaks to the tenacity of the open cell MCC length scale throughout successive diurnal cycles. This peak appears more prominent in the early morning, and extends to longer wavelengths in the later morning. This result is consistent with the diurnal cycle of cellular convection being maximum in the early morning. The nearshore closed cell region appears to be more variable. A strong peak near the 6 km wavelength exists in the morning hours, and multiple spikes at 8, 20, 15 and 29 km exist in the late morning.

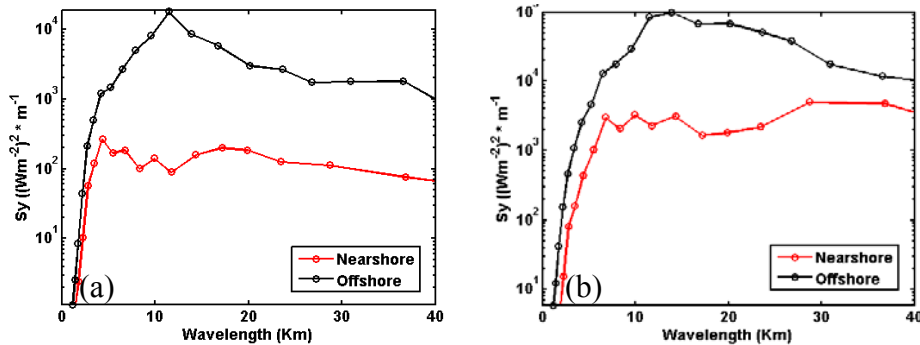


Figure 21. Area averaged PDS (a) two hours prior and (b) two hours after RF05.

### *b. RF10*

With an identical methodology used in RF05, the temporal variability during RF10 is analyzed. Figure 22 shows the GOES irradiance measurements at 1700 and 2100

GMT, two hours prior to and after RF10. As with the previous case, the STCU remains largely unchanged throughout this four hour time window. Most notably, the transition zone between the open and closed cell regions remains in the same location.

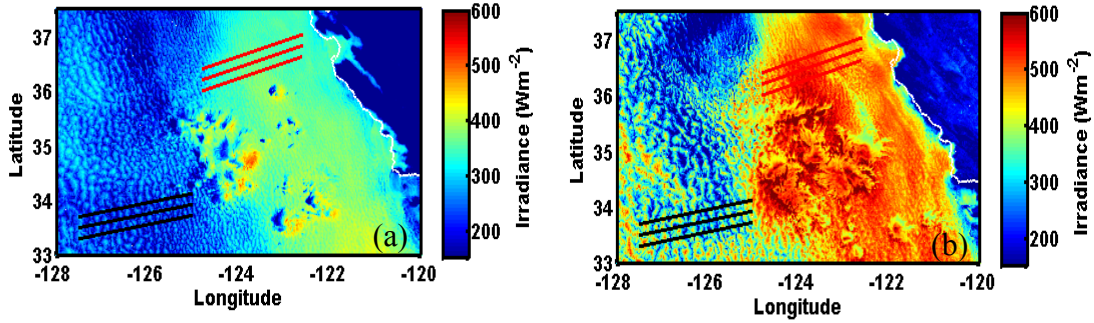


Figure 22. GOES irradiance (a) two hours prior and (b) two hours after RF10.

As shown in Figure 23, the area averaged PSD indicates that the offshore wavelength of maximum PSD varies only slightly, from 14 to 19 km through the morning. The nearshore region has a spike at the 8 km wavelength in the early morning, and it increases to 14 km by the late morning.

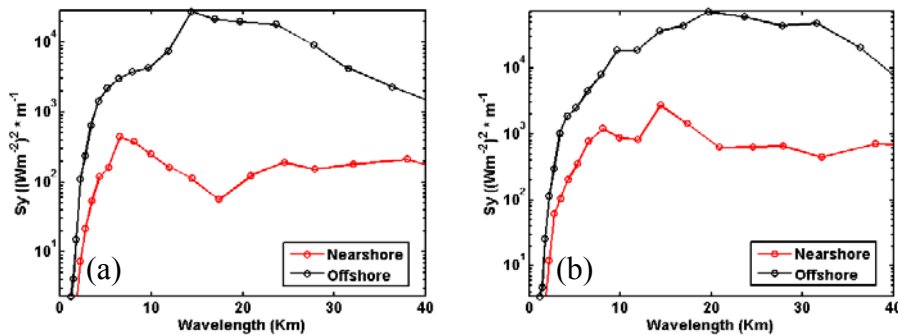


Figure 23. Area averaged PSD (a) two hours prior and (b) two hours after RF10.

A feature common to both RF05 and RF10 is that the PSD appears to shift to larger wavelengths through the morning, particularly in the nearshore closed cell region. This could be an indication of the cellular convection dominant at the smaller

wavelengths being reduced as incident shortwave radiation offsets some of the boundary layer processes that regulate the convective motions. The greater change in the nearshore region could be due to the lack of surface forcing compared with the offshore region. This logic is also consistent with the slightly more prominent energy spike that exists earlier in the morning. This suggests that convective motions, and hence cellular appearance, are more “organized” in the early morning.

Although these slight energy shifts exist, the STCU appearance and the PSD relative values remain somewhat consistent. This suggests that although the individual cellular features advect with the mean wind, the area averaged characteristics over the same location remain relatively unchanged with time. These preliminary findings on temporal variability require additional analysis.

## IV. AIRCRAFT DATA ANALYSIS

### A. DATA SELECTION METHODOLOGY

Although a variety of interesting mesoscale structures were identified in the satellite imagery, the scope will be narrowed to only those features that were thoroughly transected by the aircraft. The quantitative analysis of the imagery should have corresponding in-situ data in order to link the in-cloud dynamic and thermodynamic processes to the morphological appearance of the cloud. With nearly half of the research flights being conducted within regions of horizontally extensive closed MCC, it appears that this specific mesoscale feature will provide the largest amount of data for further analysis. Since the spatial variations of the measured variables are one of the desired outputs, flight legs that were flown at a constant heading and altitude are needed. These flight legs are known as level legs (LL). Multiple level legs within each flight are numbered sequentially (i.e., LL3). In order to have an adequately long time-series of in-cloud perturbations, we chose only the level legs that were flown entirely within the cloud layer of the STBL. Table 1 lists the specific flight legs that have these desired attributes, and will be considered for analysis.

Flight #	Date	Leg #	Heading	Altitude	Length
RF05	11SEP12	LL1	230 deg.	500 Meters	89.1 Km
RF05	11SEP12	LL3	35 deg.	500 Meters	66.5 Km
RF05	11SEP12	LL8	230 deg.	412 Meters	55.5 Km
RF10	26SEP12	LL4	80 deg.	576 Meters	91. Km
RF10	26SEP12	LL5	80 deg.	504 Meters	44.9 Km

Table 1. Twin Otter in-cloud level legs investigated.

### B. RF05 AIRCRAFT DATA ANALYSIS

The raw data for the three RF05 level legs are shown in Figures 24, 25, and 26. Three distinct scales of variation are noted in the raw data. Several of the variables exhibit a quasi-linear trend due to the relative positioning of the aircraft within the STCU cloud layer. Even though the aircraft is flying at a constant altitude throughout the flight

leg, the changing height of the boundary layer results in a slight increase or decrease in the aircraft's cloud-relative vertical position. Perturbations to the measured variables also occur as the aircraft flight path intersects the closed cell circulations identified in the satellite imagery.

The key thermodynamic variables are in good agreement through the convective downdraft regions of the MCC, with liquid water content ( $q_l$ ), water vapor ( $q$ ), and potential temperature ( $\theta$ ) all decreasing simultaneously. This is an indication of slightly dryer and colder air, resulting from the incorporation of dry air from above the boundary layer inversion into convective downdrafts, and subsequent evaporative and infrared cooling, resulting in denser and negatively buoyant air.

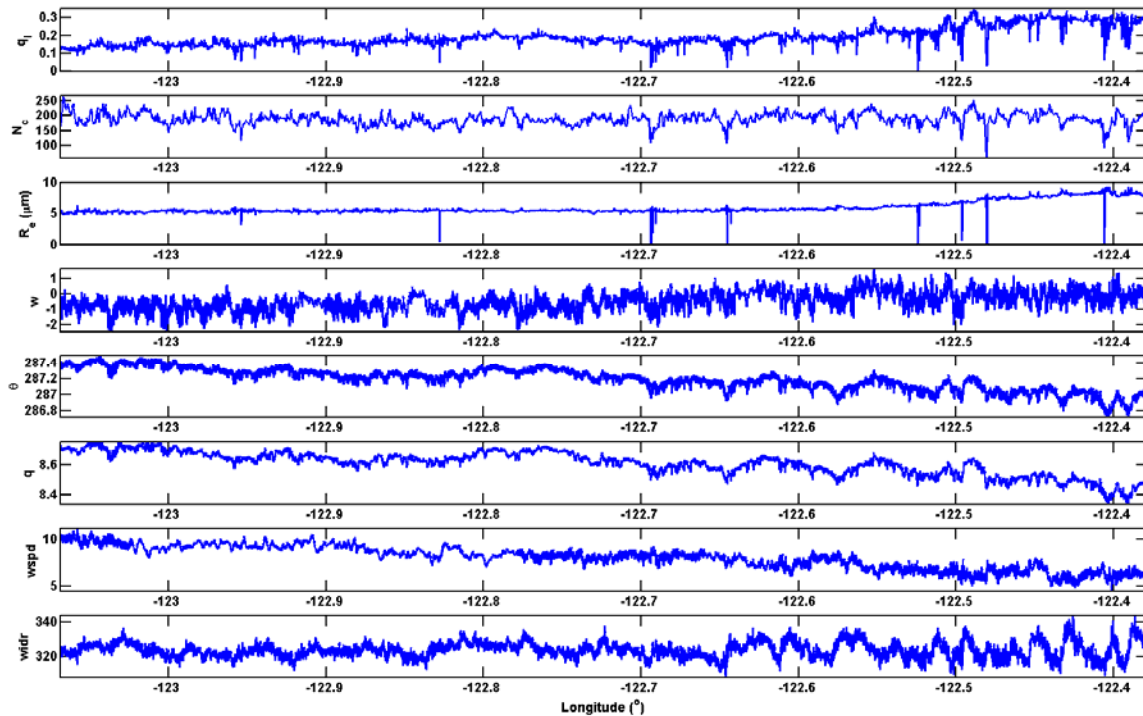


Figure 24. Spatial variations along the flight track observed from RF05 LL1.

Shown here are cloud liquid water content ( $q_l$ ), droplet number concentration ( $N_c$ ) and droplet mean effective radius ( $R_e$ ), vertical velocity ( $w$ ), potential temperature ( $\theta$ ), water vapor ( $q$ ), wind speed ( $wspd$ ) and wind direction ( $wdir$ ).

The key microphysical parameters also show agreement in the downdraft regions. The decrease in  $q_l$  is due to concurrent decreases in both the droplet concentration ( $N_c$ ) and droplet effective radius ( $R_e$ ). The decrease in droplet concentration is an indication of droplet evaporation in the entrainment parcel, which also resulted in a decrease in  $R_e$ .

The perturbations in the dynamic variables are consistent with the previously described microphysical and thermodynamic perturbations. Negative values of vertical velocity ( $w$ ) indicate downward flow in the cold and dry regions of the cloud. The wind direction plot indicates perturbations to the mean synoptic northwesterly flow. This systematic veering and backing of the mean wind is an indication of wind convergence and divergence and will be investigated further in a subsequent section.

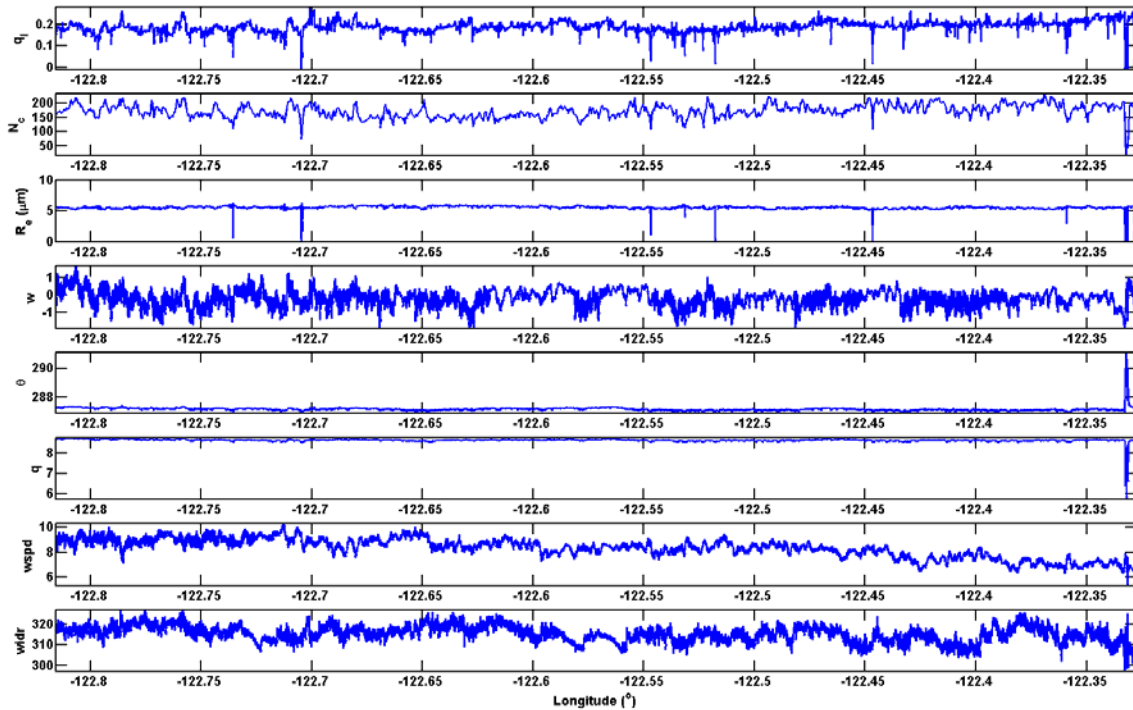


Figure 25. Same as in Figure 24, except for LL3 of RF05.

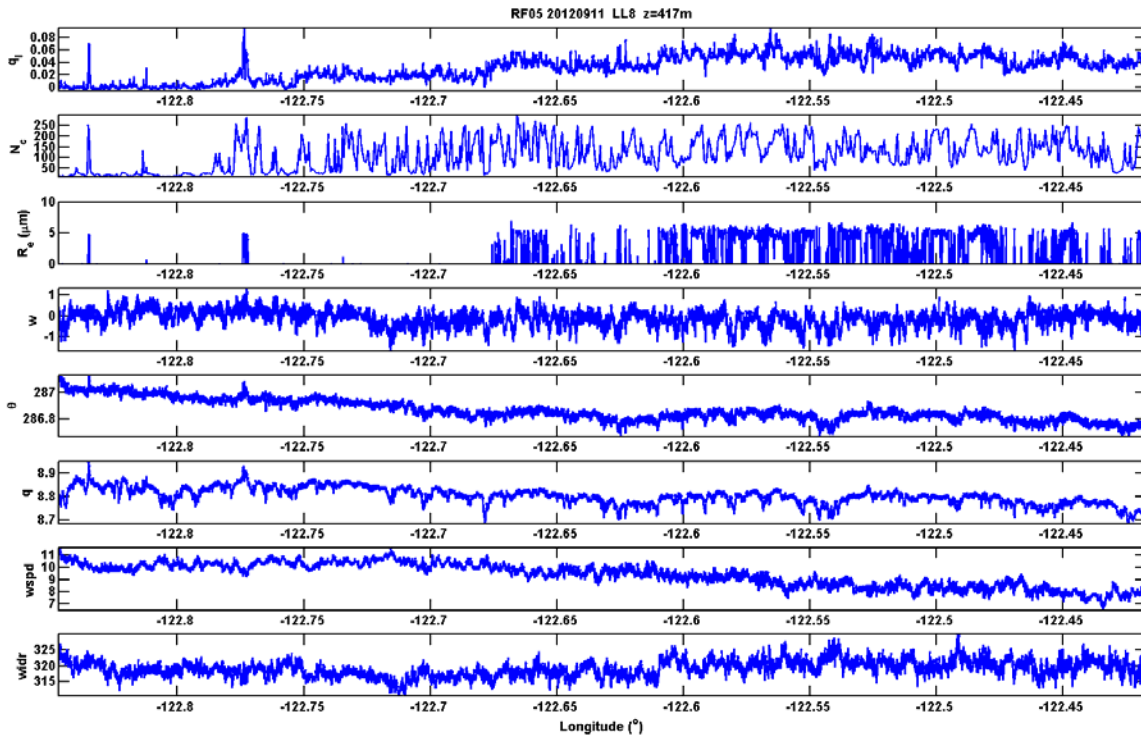


Figure 26. Same as in Figure 24, except for RF05, LL8.

When a spectral analysis is performed on these variables, the length scale of maximum PSD corresponds closely with the findings from the satellite analysis. The spectral analysis of LL1 variables shows a clear PSD spike at the 8.2 km length scale, as shown in Figure 27. The spectral analysis of LL3 and LL8 also shows a spike at the 8.2 and 10 km ranges, with additional larger PSD values at length scales larger than 20 km due to gradual variable changes not related to cloud structure. The only variable not showing a distinct spike near the 8 km length scale is the PSD for  $w$  on LL8, which indicates larger spikes at the 1.5 km and 3.8 km length scales, this result will be explained later. The results of spectral analyses are shown in Figures 27, 28, and 29. Note that the duration of the time series ( $T$ ) from each flight leg places a limit on the frequency resolution of the PSD calculations, since the frequency resolution ( $df$ ) is equal to  $1/T$ , where  $T$  is the length in time of the data section and  $f$  denotes frequency.

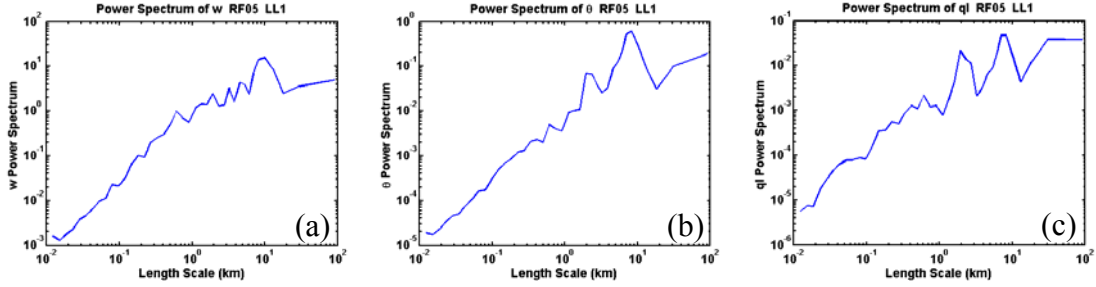


Figure 27. PSD for RF05 LL1 (a) vertical velocity (b)  $\theta$  and (c)  $q_l$ .

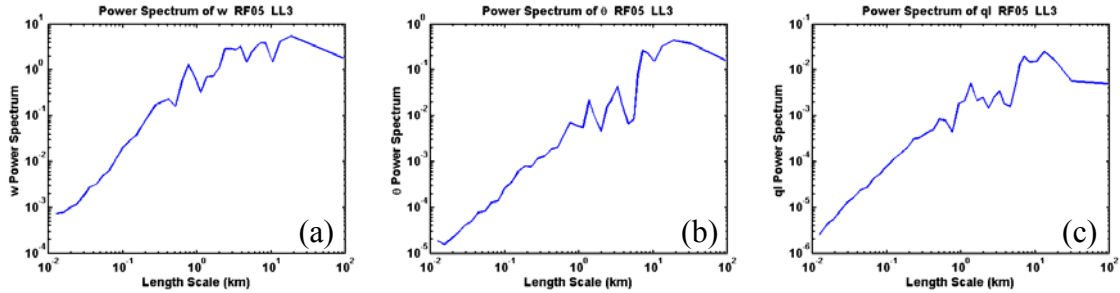


Figure 28. Same as in Figure 27, except for RF05 LL3.

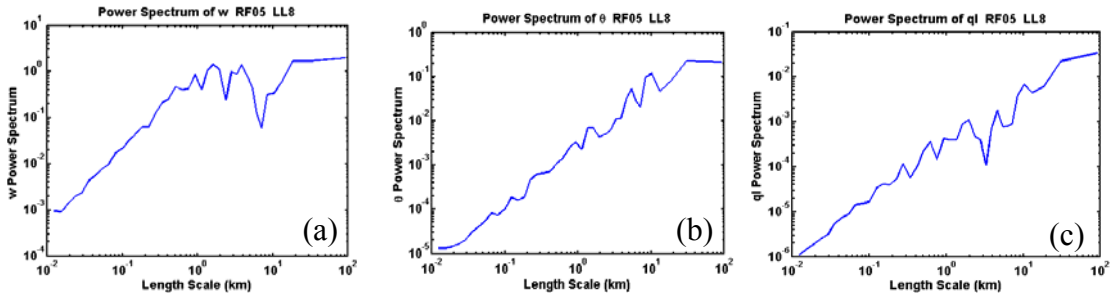


Figure 29. Same as in Figure 27, except, for RF05 LL8.

The aforementioned variable perturbations and relationships related to the cellular structure of the STCU are consistent with processes described in the background section of this thesis, and ascertained from previous studies. For this reason, further quantitative analysis of these perturbations is not conducted in order to focus on smaller scale features. As shown in Figure 30, the  $q_l$  data shows very narrow areas of significant liquid water reduction imbedded within the larger scale, sinusoidal variations due to the MCC. Conceptually, these areas are assumed to be narrow convective downdraft cloud breaks, but an analysis of their properties is needed to understand their characteristics.

In order to determine the spatial characteristics and variable properties of these features, a conditional sampling algorithm was used to identify these “events.” The algorithm used a combination of property thresholds and duration criteria to identify events. The raw data was first high pass filtered, and then areas of  $q_l$  perturbation less than  $-0.03$  were marked as events. In order to exclude noise from data spikes, the algorithm required a minimum of eight consecutive data points below the threshold in order to be identified as an event. Given the data sampling rate and aircraft speed, this translates to an approximate event minimum width of 50 meters. The choice of these threshold values for liquid water and for event width is based on multiple testing of the algorithm applied to the relevant dataset to ensure that the threshold can help select the majority of the events that show within event correlation of the various thermodynamic variables.

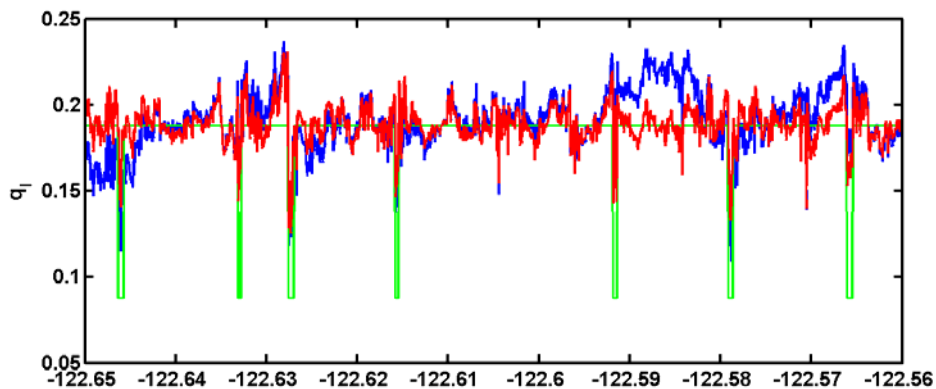


Figure 30. Example of cloud break “events” indicated by a green gate function. The original liquid water content is shown in blue, high-pass filtered  $q_l$  is shown in red.

Figure 30 shows that the identified events (indicated by the green gate function) appear to occur with a preferred spacing between events and a preferred width of event. To determine the magnitudes of these scales statistically, the probability density functions (PDF) were calculated for the respective quantities. Results for RF05 are shown in Figures 31 and 32. We found from this flight, that the distance between adjacent events is almost always less than five km, and is most often less than one km. This distance

represents the spacing between cloud breaks. The PDF for the width of the cloud break indicates a peak between 50 and 100 meters, and all of the events were less than 300 meters wide.

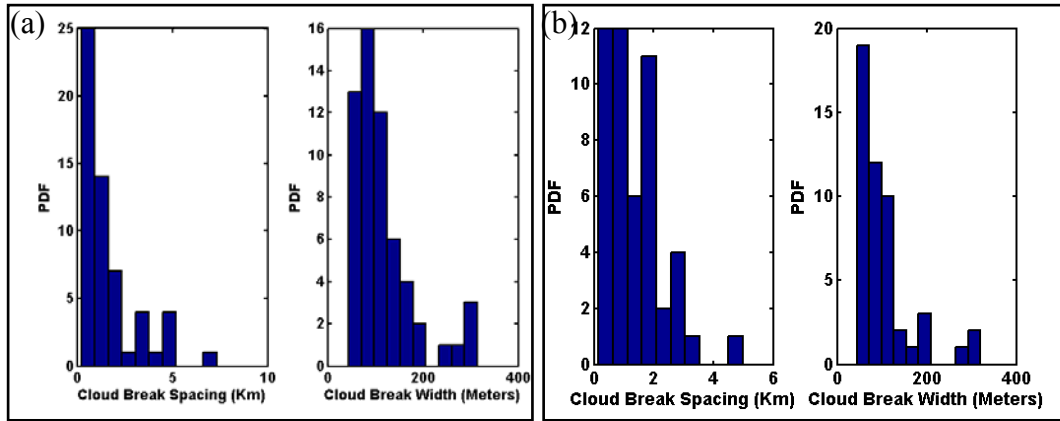


Figure 31. Event spatial characteristic PDFs for RF05. (a) LL1 and (b) LL3.

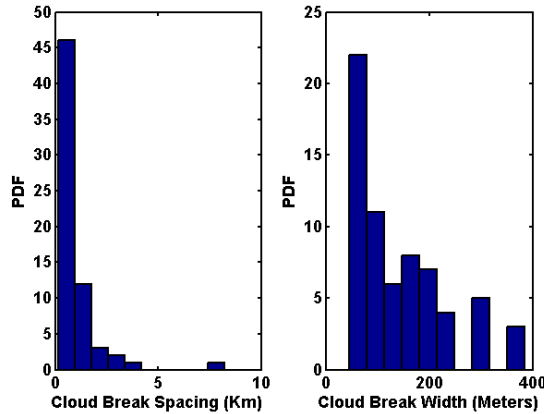


Figure 32. Event spatial characteristic PDF for RF05 LL8.

These statistical spatial characteristics indicate that these events occur at preferred length scales. The event spacing length scale is likely responsible for the secondary PSD spike observed at the one to two km length scale. This result indicates the existence of two discrete scales of variation within the closed cell MCC: turbulent scale cloud breaks imbedded within mesoscale circulations.

The thermodynamic and dynamic properties of these cloud break events are discussed here. As shown in Figure 33, the properties of these events are relatively consistent. The algorithm identified 58 events within LL1 with a mean  $w$  perturbation of  $-0.12 \text{ ms}^{-1}$ , a mean  $q$  perturbation of  $-0.01 \text{ gkg}^{-1}$ , a mean  $q_l$  perturbation of  $-0.03 \text{ gkg}^{-1}$ , and a mean  $\theta$  perturbation of  $-0.03 \text{ K}$ . These variables indicate that these cloud break events contain cool, dry, downward flowing air, consistent with what was observed in the original spatial series plots shown earlier (e.g., Figure 24).

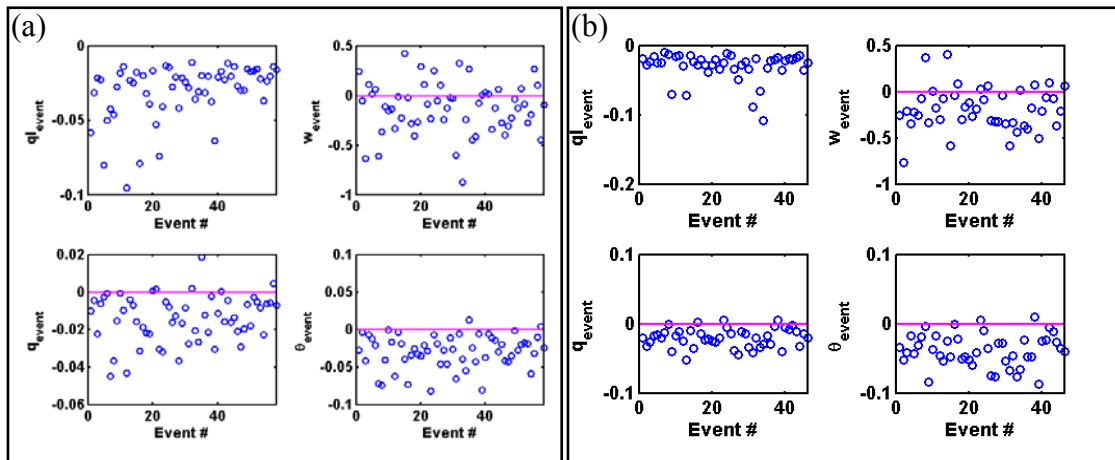


Figure 33. Event property characteristics for RF05 (a) LL1 and (b) LL3.

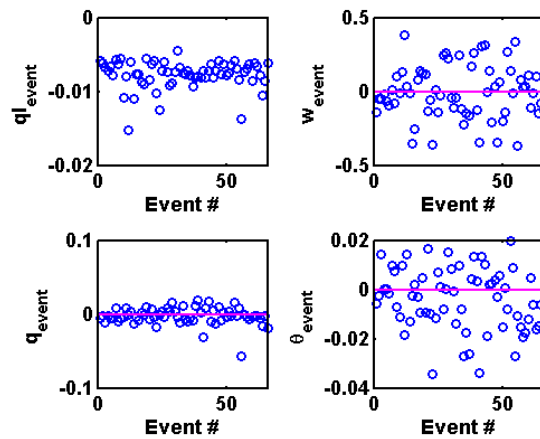


Figure 34. Event property characteristics for RF05 LL8.

The conditional sampling algorithm identified 50 events within LL3 with a mean  $w$  perturbation of  $-.18 \text{ ms}^{-1}$ , a mean  $q$  perturbation of  $-.03 \text{ gkg}^{-1}$ , a mean  $q_l$  perturbation of  $-.03 \text{ gkg}^{-1}$ , and a mean  $\theta$  perturbation of  $-.01 \text{ K}$ . Although these perturbations appear small, note that these perturbations represent a 10–20 percent reduction in moisture, compared to the surroundings. With LL1 and LL3 flown at the same altitude, and LL3 only 20 km downstream from LL1, the events have similar variable perturbations.

LL8 was flown 100 meters below LL3, so we expect some vertical variations in the event property characteristics as the convective downdraft progresses downward through the STCU layer. Note that conditional sampling threshold for  $q_l$  was reduced from .03 to .01 for LL8 to account for the reduced  $q_l$  values near the cloud base. The algorithm identified 66 events within LL8 with a mean  $w$  perturbation of  $-.006 \text{ ms}^{-1}$ , a mean  $q$  perturbation of  $-.002 \text{ gkg}^{-1}$ , a mean  $q_l$  perturbation of  $-.008 \text{ gkg}^{-1}$ , and a mean  $\theta$  perturbation of  $-.004 \text{ K}$ . The magnitude of these perturbations are significantly smaller compared to those from the legs above, however, they still consistently suggest cool downdrafts with depleted cloud water. This strong reduction in the magnitude of the perturbations of these variables with decreasing height within the STCU layer can be attributed to the mixing of adjacent warmer and moister air into the downdraft. Since the downdrafts' thermodynamic properties are now more similar to the horizontal surroundings, this results in a reduction in the negative buoyancy of the downdraft, and reduced negative vertical velocity.

The relationship between dynamic and thermodynamic variable perturbations within these events will be investigated here. Shown in Figures 35 and 36, the correlation between dynamic and thermodynamic properties within events is linearly correlated, which is more apparent between water vapor, potential temperature and vertical velocity. The corresponding correlation coefficients are given in Table 2, which show that the correlation coefficients are mostly positive, and between .1 and .7. This is an indication of a typically cooler and drier air within downdraft regions. Table 2 also shows a strong reduction in the magnitude of variable perturbations lower in the cloud level (LL8), this is an indication of the cloud breaks mixing with the environment further away from the cloud top.

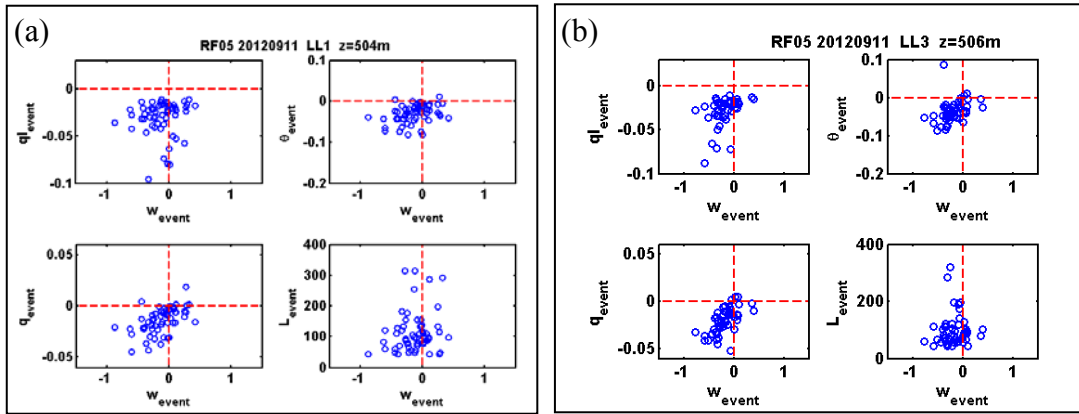


Figure 35. Correlation of event properties with event mean vertical velocity for RF05 (a) LL1 and (b) LL3.

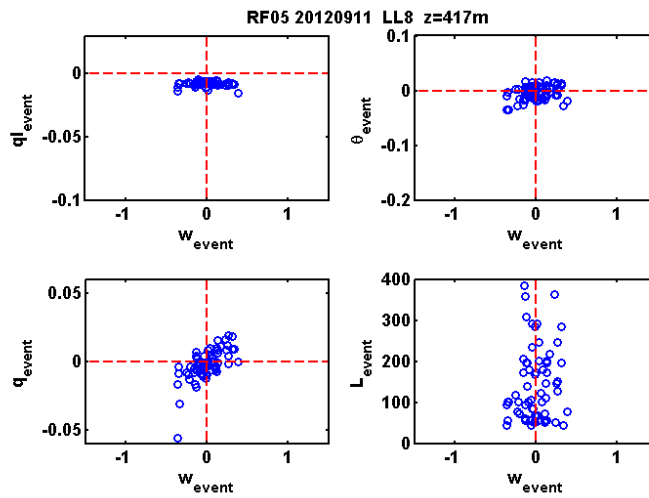


Figure 36. Variable relationship for RF05 LL8.

	$R_{wq}$	$R_{w\theta}$	$R_{wql}$	$w_{event}$	$\theta_{event}$	$q_{event}$	$q _{event}$
LL1	.5243	.3450	.0816	-.2499	-.0322	-.017	-.030
LL3	.0703	.0957	.2324	-.2745	-.0114	-.043	-.036
LL8	.6731	.2729	-.0450	-.1323	-.006	-.007	-.007

Table 2. Correlation coefficients between event averaged vertical velocity and water vapor,  $\theta$ , and liquid water and event mean perturbations from each leg.

As noted before, the raw horizontal wind data indicated a slight veering and backing that appeared to be related to the identified cloud breaks/downdrafts. To investigate this further, the wind direction and wind speed was used to calculate the along

track component of the horizontal wind vector. By determining along track changes to the along track wind component, the confluence or diffluence of the horizontal wind is determined. It's important to note that horizontal convergence and divergence cannot be precisely known, since across track variation in the across track component of the wind cannot be calculated from a one dimensional aircraft transect.

Figure 37 shows vertical velocity and the horizontal wind confluence from LL1 of RF05. It is seen that the strong downdrafts are often associated with wind confluence with a correlation coefficient for these two variables being 0.25. If we assume that the horizontal wind confluence observed here indicates horizontal wind convergence, their correlation with vertical velocity is consistent with mass conservation and hence physically plausible. In other words, the horizontal convergence is a result of cloud breaks being strong developing downdrafts. At LL8, lower in the cloud layer, the correlation coefficient between vertical velocity and horizontal confluence is -0.1. This is another indication of a decreasing magnitude of the negative vertical velocity as the downdraft progresses through the STCU layer.

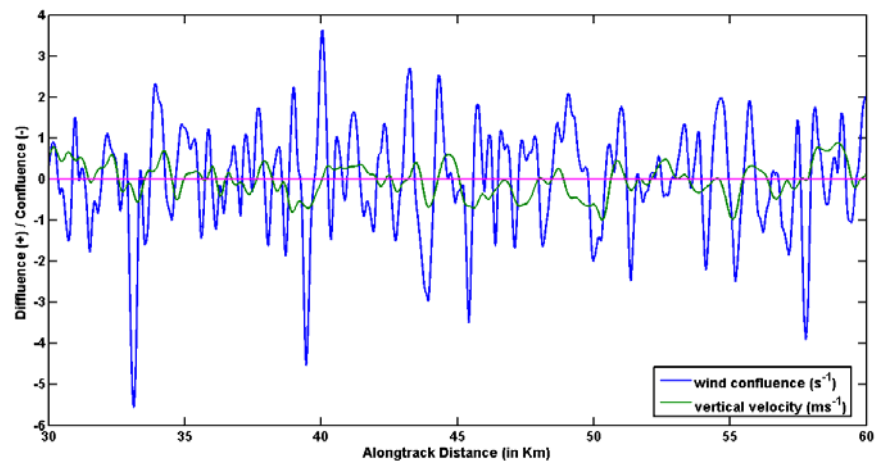


Figure 37. LL1 wind confluence and vertical wind plot.

When the PSD of the horizontal wind confluence is calculated, a distinct spike at the 1.5 to 3 km length scale exists, as shown in Figure 38. Since these are the same length scales previously identified with the spatial characteristics of the downdraft events, this is

an indication that these phenomena are related. This is consistent with the observed reduction in the magnitudes of variable perturbations as the downdraft progresses through the STBL. These variable perturbations are reduced via horizontal mixing (i.e., horizontal wind confluence) with adjacent air with different variable properties. This confirms the linkage between dynamic and thermodynamic processes in the cloud breaks.

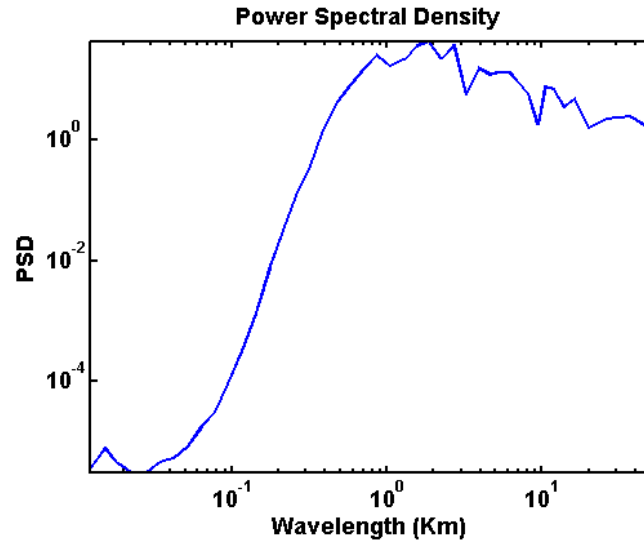


Figure 38. PSD for wind confluence on LL1.

In order to determine the contribution to vertical fluxes from different length scales, the co-spectra between vertical velocity and thermodynamic and cloud variables were calculated. As shown in Figure 39, all of the calculated co-spectrum for LL1 indicates distinct spikes at the 0.6, 1.9 and 8.2 km length scales. The strong relationship between  $w$  and the thermodynamic variables at these specific length scales is an indication of strong temperature and moisture fluxes associated with the MCC circulations (8.2 km), and the narrow imbedded downdraft events within the MCC (0.6 km and 1.9 km event spacing) The co-spectra for LL3 (Figure 40) looks slightly different. It shows a broad spike in the 8–30 km length scales, and three other spikes at the 0.75, 1.3 and 3.2 km length scales. The most notable difference in LL3 is the much smaller magnitude in the 8–10 km length scales, which suggests reduced fluxes associated with MCC circulations. The fluxes associated with narrow convective downdraft events

appear near the same length scales and at similar magnitudes. Since LL8 was flown lower in the cloud layer, its Co-spectrum indicates reduced fluxes across all length scales although enhanced covariance are still noticeable at the length scales associated with MCC and narrow downdrafts, indicating that modest fluxes are still occurring. A notable difference is that the co-spectrum for  $w$  and  $q_1$  reverses sign at the 0.6 km length scale. The representativeness of this result should be studied with more measurements to reach any physical explanations.

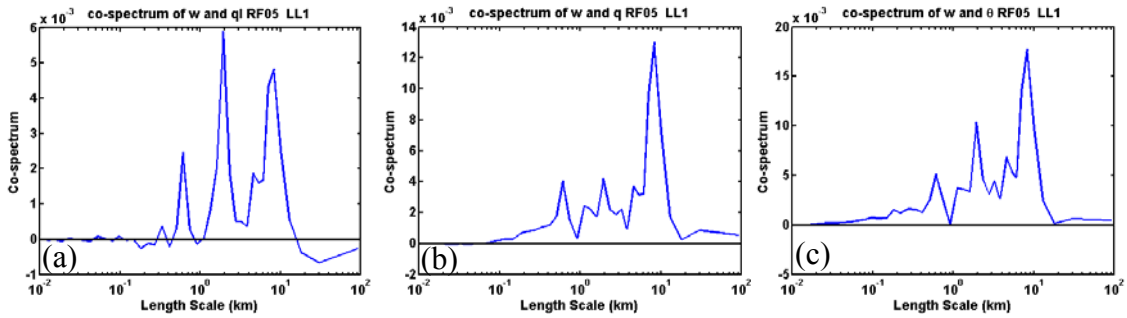


Figure 39. RF05 LL1 Co-spectrum of (a)  $w$  and  $q_1$  (b)  $w$  and  $q$  (c)  $w$  and  $\theta$ .

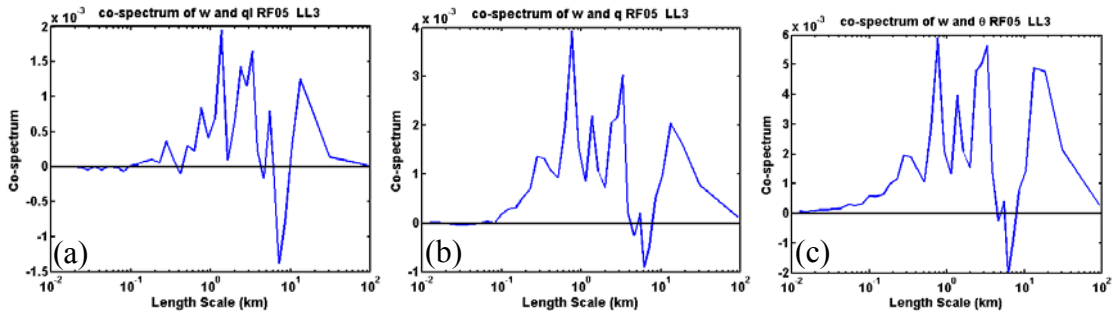


Figure 40. RF05 LL3 Co-spectrum of (a)  $w$  and  $q_1$  (b)  $w$  and  $q$  (c)  $w$  and  $\theta$ .

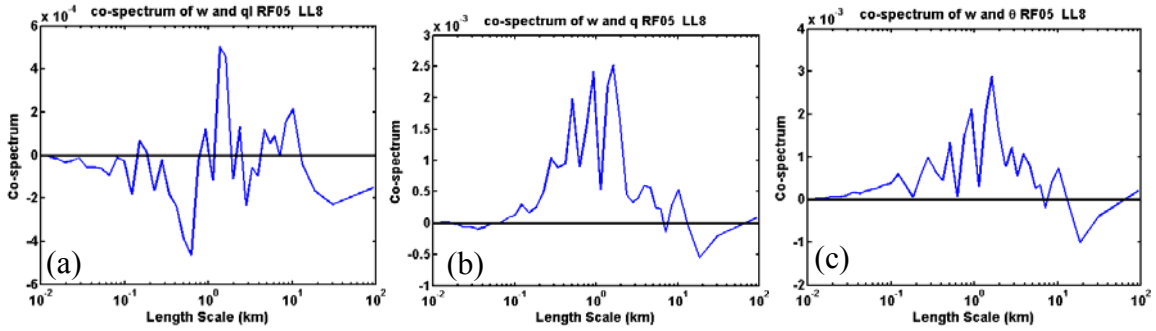


Figure 41. RF05 LL8 Co-spectrum of (a)  $w$  and  $q_l$  (b)  $w$  and  $q$  (c)  $w$  and  $\theta$ .

### C. RF10 AIRCRAFT DATA ANALYSIS

Using the same method as in RF05, the measurements from RF10 are analyzed and the results are presented here. Figures 42 and 43 show the spatial variation of various key variables for LL4 and LL5 of RF10. These measurements show similar perturbations and correlations among different variables seen in the in-cloud legs of RF05. A notable difference is that the extreme western portion of LL4 was flown through a few open cell MCC, hence the larger perturbations in variables in this portion of the flight leg.

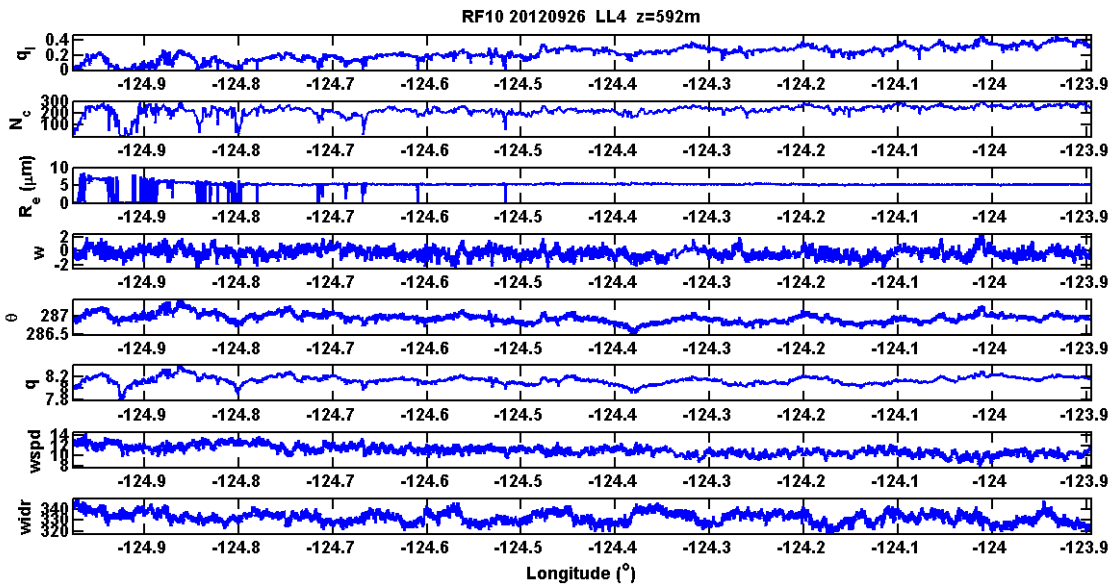


Figure 42. Same as in Figure 24, except for RF10 LL4.

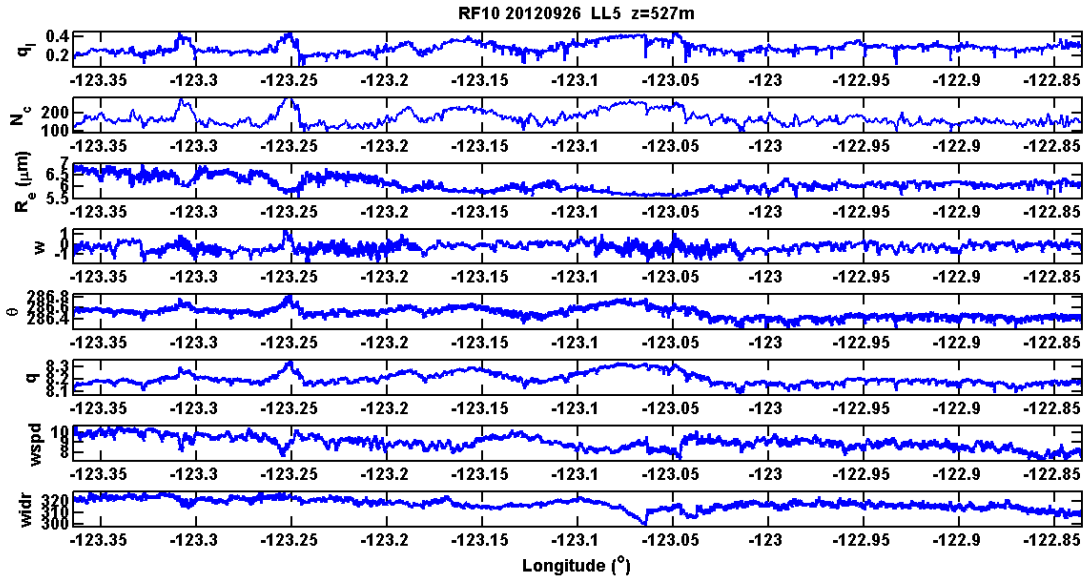


Figure 43. Same as in Figure 24, except for RF10 LL5

When the PSD from these flight legs is calculated, we see a strong peak in the 8 to 10 km length scales. This length scale corresponds well with our spectral analysis of the satellite identified closed cell MCC in this region, and closely matches the length scale identified in RF05. Similar to RF05, we see smaller secondary peaks at smaller length scales that are related to narrow cloud breaks. Also similar to RF05, the PSD for  $w$  on LL5 is showing more energy at the 1.8 km and 5 km scales than it is at the larger length scales, this is also an indication of strong narrow downdraft regions.

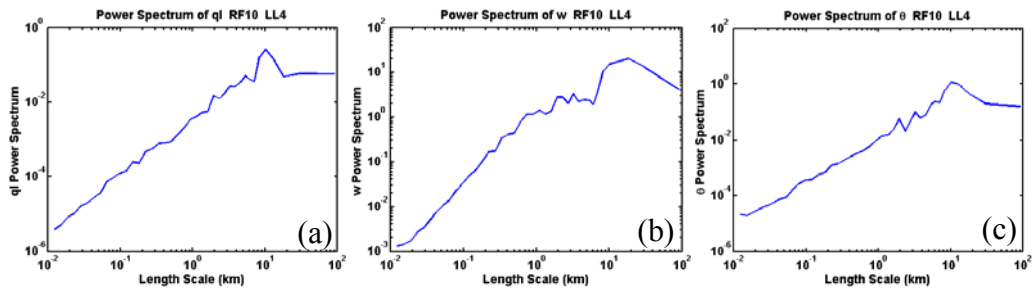


Figure 44. PSD calculation for RF10, LL4 (a)  $q_l$  (b)  $w$ , and (c)  $\theta$ .

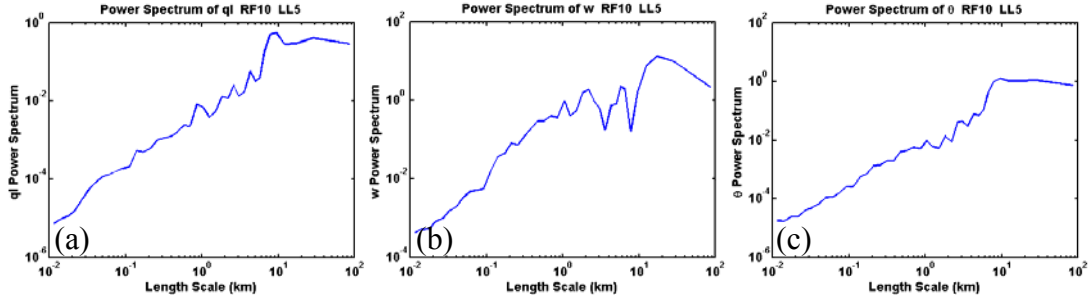


Figure 45. PSD calculation for RF10, LL5 (a)  $q_l$  (b)  $w$ , and (c)  $\theta$ .

Figure 46 shows the PDFs of length scales associated with the identified cloud breaks from in-cloud measurements of the Twin Otter and using the conditional sampling method. Results for LL4 indicate that the distance between adjacent events is less than 4 km, and is most often less than one km. The PDF for the cloud break width indicates that the majority of events have widths between 50 and 100 meters, and all of the events were less than 300 meters wide. These spatial characteristics are very similar to the findings from RF05.

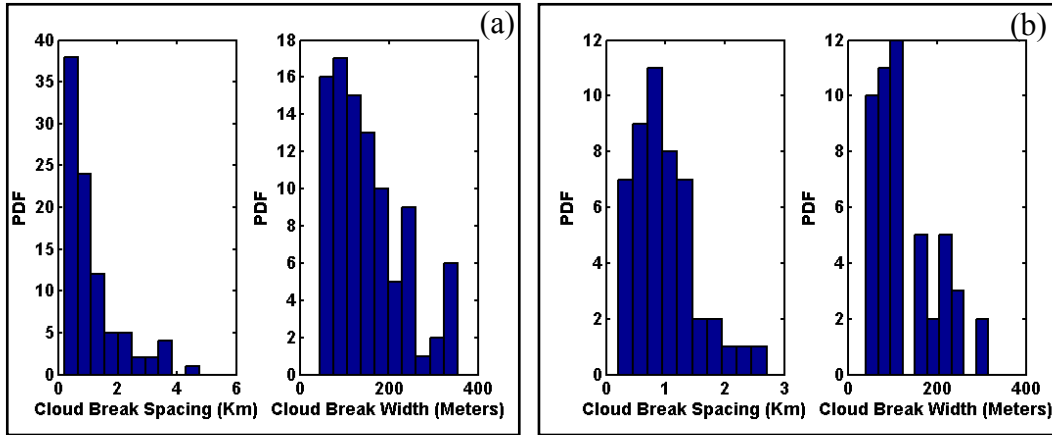


Figure 46. Spatial characteristics for cloud break events in RF10 (a) LL4 and (b) LL5.

Figure 47 shows the correlation between the dynamic and thermodynamic properties of the identified events. We find the same general properties identified in RF05. In LL4, we identified 94 events with a mean  $w$  perturbation of  $-0.14 \text{ ms}^{-1}$ , a mean  $q$

perturbation of  $-0.01 \text{ gkg}^{-1}$ , a mean  $q_l$  perturbation of  $-0.03 \text{ gkg}^{-1}$ , and a mean  $\theta$  perturbation of  $-0.03 \text{ K}$ . In LL5, the algorithm identified 50 events within LL5 with a mean  $w$  perturbation of  $-0.12 \text{ ms}^{-1}$ , a mean  $q$  perturbation of  $-0.01 \text{ gkg}^{-1}$ , a mean  $q_l$  perturbation of  $-0.03 \text{ gkg}^{-1}$ , and a mean theta perturbation of  $-0.03 \text{ K}$ . These perturbations are consistent with findings from RF05, and once again indicate cool, dry, downdrafts.

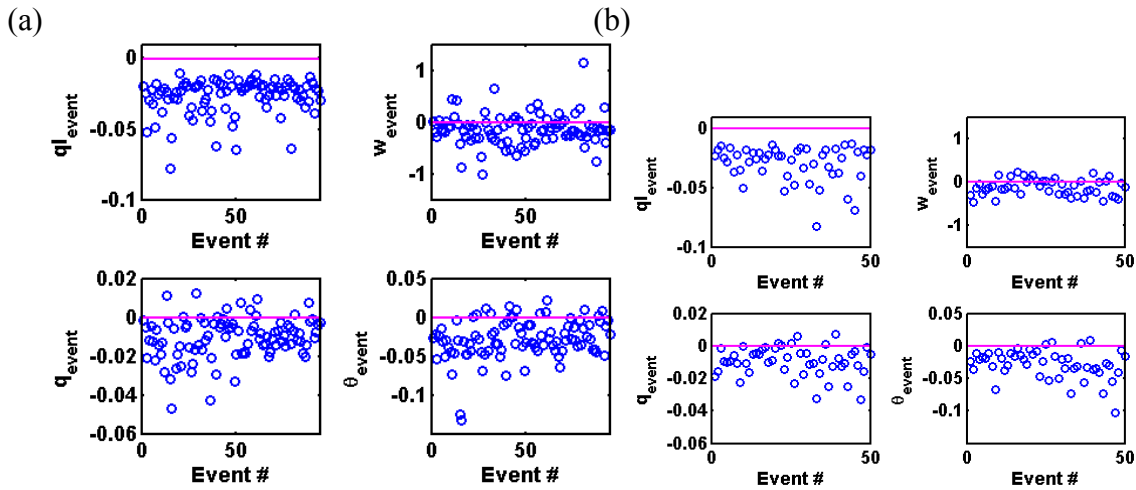


Figure 47. Event property characteristics for RF10 (a) LL4 and (b) LL5.

As shown in Figure 48 and Table 3, the dynamic and thermodynamic perturbations have a weak linear correlation, with correlation coefficients ranging from 0.1 to 0.6. With results similar to RF05, this tells us that although all events averaged together are typically characterized by negative variable perturbations, an extreme amount of variability can exist within any single event.

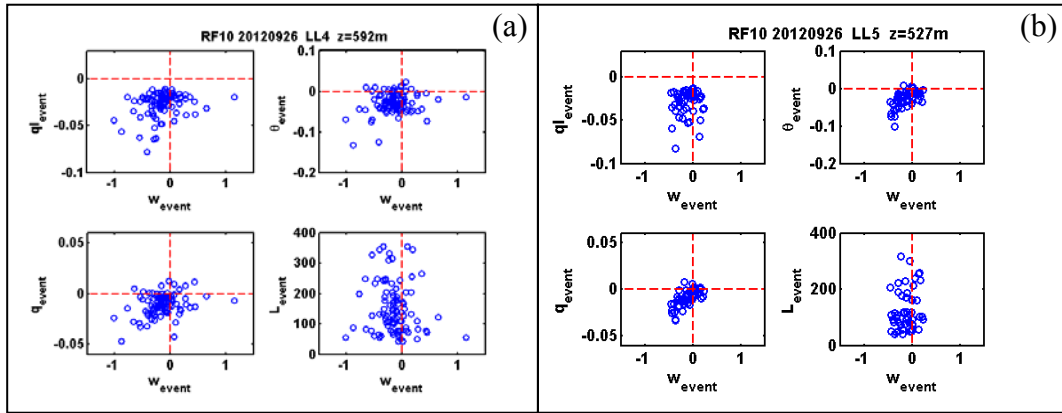


Figure 48. Variable relationship for RF10 (a) LL4 and (b) LL5

	$R_{wq}$	$R_{w\theta}$	$R_{wql}$	$W_{event}$	$\theta_{event}$	$q_{event}$	$q_{levent}$
LL4	.3224	.2368	.2756	-.2594	-.0291	-.011	-.028
LL5	.6528	.5960	.1197	-.2149	-.0333	-.012	-.029

Table 3. Correlation coefficients and downdraft perturbation values.

The veering and backing of horizontal winds was analyzed to determine the scales of horizontal wind variation, particularly associated with the confluence of wind in the cloud breaks. The PSD of wind confluence for LL4 (Figure 49) indicates distinct peaks at the 1, 5.3, and 10 km length scales. The PSD of wind confluence for LL5 indicates distinct peaks at the 1, 2.5, and 7.5 km length scales. These results match closely with previously identified scales of variation for MCC, and the narrow downdraft regions.

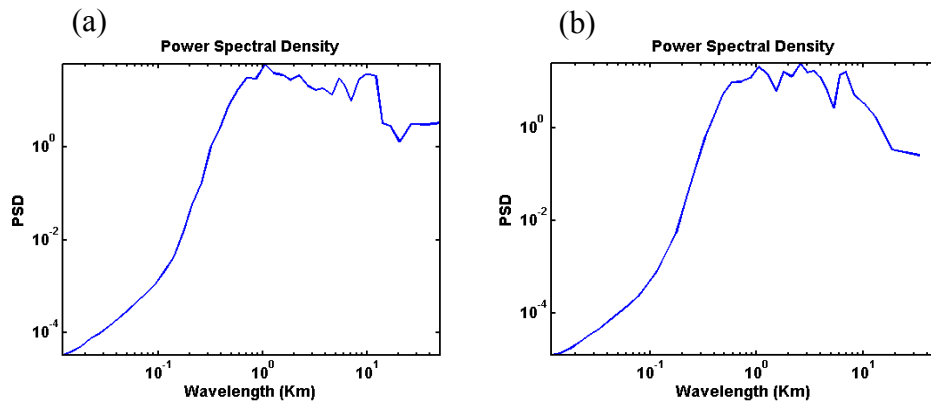


Figure 49. PSD for wind confluence on RF10 (a) LL4 and (b) LL5.

Similar to RF05, there appears to be vertical changes to the horizontal winds relationship to the vertical wind. During the early section of LL3, near the cloud base, the horizontal wind divergence and the vertical velocity have a correlation coefficient of -0.15. This is an indication of a horizontal wind divergence driven by vertical convergence resulting from downdraft stalling. Later in LL3, near the center of the cloud layer, the correlation coefficient becomes 0.26, indicating a horizontal convergence of air in the wake of accelerating downdrafts. These findings are identical to RF05 findings in LL3 (near center of cloud layer) and LL8 (near cloud base).

When the co-spectra between vertical velocity and thermodynamics of cloud variables are calculated for LL4, three distinct peaks are shown at the 1 km, 2-3km and 10 km length scales. Similar to RF05, these length scales are consistent with increased temperature and moisture fluxes associated with MCC, and narrow downdraft events. The co-spectra for LL5 show good agreement in the shorter lengths scales, but changes signs between the 5 to 17 km length scale. Results from LL4 and LL5 on this larger scale are inconsistent. Considering the close proximity of LL4 and LL5 this result is unexpected. It is possible that the short length of the legs does not provide the needed length for good statistics and warrants some future in-depth analyses.

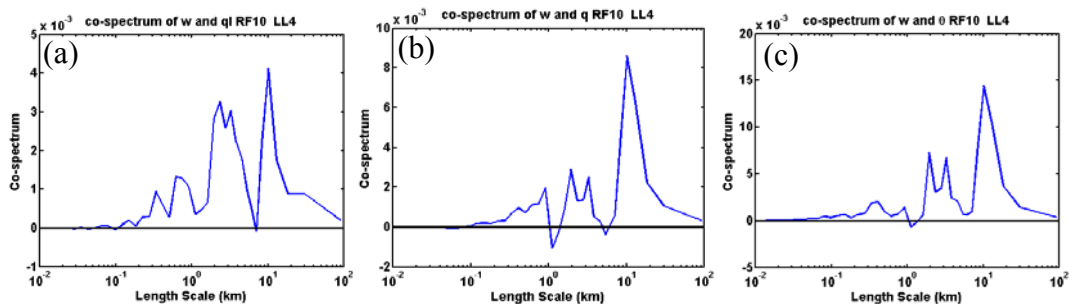


Figure 50. RF10 LL4 Co-spectrum of (a)  $w$  and  $q_1$  (b)  $w$  and  $q$  (c)  $w$  and  $\theta$ .

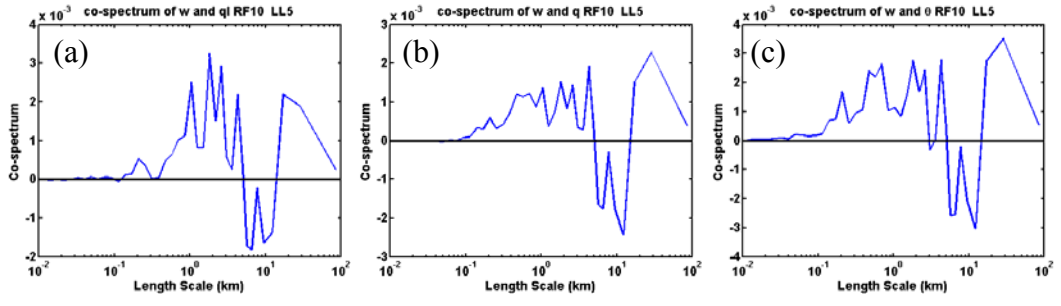


Figure 51. RF10 LL4 Co-spectrum of (a)  $w$  and  $ql$  (b)  $w$  and  $q$  (c)  $w$  and  $\theta$ .

## V. DISCUSSION

### A. SUMMARY AND CONCLUSIONS

Central California's coastal stratocumulus layer was measured with an instrumented aircraft during the UPPEF 2012 experiment. This study analyzed the in-cloud level leg measurements from two of the 12 flights of UPPEF: RF05 and RF10. During these two flights, the horizontally extensive stratocumulus layers exhibited closed cell MCC near the coast, and transitioned to open cell MCC further offshore. Analysis of satellite imagery suggests uniform area averaged spatial characteristics within these regions. The nearshore closed cell MCC region had a dominant length scale of 8.5 km, which was consistent between different days. The offshore open cell region exhibited larger length scales of 12 km and 20 km.

Aircraft transects conducted through the closed cell MCC STCU layers exhibited variable perturbations on two distinct length scales. Perturbations associated with MCC occurred at length scales identical to the satellite observations. Perturbations also occurred on smaller length scales due to narrow, sub-kilometer convective downdrafts imbedded within the MCC, which are first identified by smaller-scale cloud breaks. These events showed less spatial organization than MCC, with the distance between events ranging from .5 km to 3 km, and typical event widths of 1 km or less. Although variable perturbations in any individual event varied greatly, typical event perturbations include colder, dryer, downward flowing air. Analysis of dynamic and thermodynamic variables has shown that downdraft velocity typically increases in the top/middle cloud layer, but subsequent horizontal mixing of adjacent air reduces the magnitude of downdraft variable perturbations, reduces negative buoyancy, and slows the downdraft near cloud base. Despite the small scale of these narrow downdrafts, they appear to provide a large contribution to the vertical flux of moisture and temperature within the boundary layer.

## **B. RECOMMENDATIONS FOR FUTURE RESEARCH**

Our initial analysis of the temporal variability of the coastal STBL has revealed some possible diurnal variations in the satellite observed length scales of the coastal MCC. Although we suspect this may be related to radiative forcing and the associated variations in surface and cloud top fluxes, a more robust analysis of satellite imagery and comparison with in-situ measurements throughout a larger time window is required to determine the feedback processes involved in such diurnal variation.

This thesis identified two distinct scales of variation due to MCC and narrow downdrafts occurring within the MCC. The interaction of these phenomena needs further analysis. Our analysis has shown that narrow convective downdrafts do not always occur within the larger MCC downdraft regions, they can occur within the MCC updraft region. It is assumed that for the MCC circulations to persist, the narrow downdrafts would have to occur in the MCC downdraft regions more often, but a statistical analysis of downdraft event location would have to be undertaken to prove this. This study of scale interactions could have implications for the temporal evolution of MCC.

## LIST OF REFERENCES

- Abdul-Razzak, H., and C. Rivera-Carpio, 1998: A parameterization of aerosol activation. 1. Single aerosol type. *J. Geophys. Res.*, **103** (D6), 6123–6131.
- Bergman, J. W., and M. L. Salby, 1996: Diurnal variations of cloud cover and their relationship to climatological conditions. *J. Climate*, **9**, 2802–2820.
- Bretherton, C. D., T. Uttal, C. W. Fairall, S. E. Yuter, R. A. Weller, D. Baumgardner, K. Comstock, and R. Wood, 2004: The EPIC 2001 stratocumulus study. *Bull. Amer. Meteor. Soc.*, **85**, 967–977.
- Climate change, 2009. [Available online at <http://greenfleet.dodlive.mil/climate-change/>]
- Deardorff, J. W., 1980: Cloud top entrainment instability. *J. Atmos. Sci.*, **37**, 561–563.
- Engeln, A., and J. Teixeira, 2004: A ducting climatology derived from ECMWF global analysis fields. *Journal of Geophysical Research*, **109**, 1–18.
- Goodman, J., 1977: The microstructure of California coastal fog and stratus. *Journal of Applied Meteorology*, **16**, 1056–1067.
- Hanson, H. P., 1991: Marine stratocumulus climatologies. *Int. J. Climatol.*, **11**, 147–164.
- Hubert, L. F., 1966: *Mesoscale Cellular Convection*. Meteorological Satellite Laboratory Report No. 37, U. S. Dept. of Commerce, Environmental Science Services Administration, 68 pp.
- Klein, S. A., and D. L. Hartmann, 1993: The seasonal cycle of low stratiform clouds. *J. Climate*, **6**, 1588–1606.
- Krueger A. F. and S. Fritz, 1960: Cellular cloud patterns revealed by Tiros I. *Tellus: A quarterly Journal of Geophysics*, **13**, 1.
- Leon, D. C., Z. Wang, and D. Liu, 2008: Climatology of drizzle in marine boundary layer clouds based on 1 year of data from CloudSat and Cloud-Aerosol Lidar and Infrared Pathfinder Satellite observations (CALIPSO). *J. Geophys. Res.*, **113**.
- Liou, K. N., 1992: *Radiation and Cloud Processes in the Atmosphere: Theory, Observation and Modeling*. Oxford University Press, 504 pp.
- Martin, G. M., D. W. Johnson, and A. Spice, 1994: The measurement and parameterization of effective radius of droplets in warm stratocumulus clouds. *J. Atmos. Sci.*, **51**, 1823–1842.

- Moyer, K. A., and G. S. Young, 1994: Observations of mesoscale cellular convection from the marine stratocumulus phase of fire. *Bound.-Layer Meteor.*, **71**, 109–134.
- Nicholls, S., 1984: The dynamics of stratocumulus: Aircraft observations and comparisons with a mixed layer model. *Quart. J. Roy. Meteor. Soc.*, **110**, 783–820.
- Nicholls, S., J. Leighton, 1985: An observational study of the structure of stratiform cloud sheets: Part I. Structure. *Quart J.R. Met. Soc.*, **112**, 431-460.
- Noonkester, V., 1984: Droplet spectra observed in marine stratus cloud layers. *Journal of Atmospheric Science*, **41**, 829-845.
- Norris, J. R., and S. A. Klein, 2000: Low cloud type over the ocean from surface observations. Part III: Relationship to vertical motion and the regional synoptic environment. *J. Climate*, **13**, 245–256.
- Pincus, R., and M. B. Baker, 1997: What Controls Stratocumulus Radiative Properties? Lagrangian Observations of Cloud Evolution. *J. Atmos. Sci.*, **54**, 2215–2235.
- Rothermel, J., and E. M. Agee, 1980: Aircraft investigation of mesoscale cellular convection during AMTEX75. *J. Atmos. Sci.*, **37**, 1027–1040.
- Schubert, W. H., J. S. Wakefield, E. J. Steiner, and S. K. Cox, 1979a: Marine stratocumulus convection. Part I: Governing equations and horizontally homogeneous solutions. *J. Atmos. Sci.*, **36**, 1286–1307.
- Slingo, A., and H. M. Schrecker, 1982: On the shortwave radiative properties of stratiform water clouds. *Quart. J. Roy. Meteor. Soc.*, **108**, 407–426.
- Slingo, A., 1989: A GCM parameterization for the shortwave properties of water clouds. *J. Atmos. Sci.*, **46**, 1419–1427.
- Stevens, B. and coauthors, 2005: Evaluation of large-eddy simulations via observations of nocturnal marine stratocumulus. *Mon. Wea. Rev.*, **133**, 1443–1462.
- Tellado, P. A., 2013: Physical processes in coastal stratocumulus clouds from aircraft measurements during UPPEF 2012. M.S., Naval Postgraduate School
- Twomey, S., 1959: The nuclei of natural cloud formation. Part II: The supersaturation in natural clouds and the variation of cloud droplet concentration. *Geofis. Pura Appl.*, **43**, 243–249.
- Warren, S. G., C. J. Hahn, J. London, R. M. Chervin, and R. L. Jenne, 1986: Global distribution of total cloud cover and cloud types over land. NCAR Tech. Note NCAR/TN-2731STR, National Center for Atmospheric Research, 29 pp.

- Wang, S., and G. Feingold, 2003: Turbulence, condensation, and liquid water transport in numerically simulated nonprecipitating stratocumulus clouds. *J. Atmos. Sci.*, **60**, 262–278.
- Wood, R., 2012: Review: Stratocumulus clouds. *Monthly Weather Review*, **40**, 2373–2423.
- Wood, R., and C. S. Bretherton, 2004: Boundary layer depth, entrainment, and decoupling in the cloud-capped subtropical and tropical marine boundary layer. *J. Climate*, **17**, 3576–3588.
- Zhu, P. and Coauthors, 2005: Intercomparison and interpretation of single-column model simulations of a nocturnal stratocumulus topped marine boundary layer. *Mon. Wea. Rev.*, **133**, 2741–2758.

THIS PAGE INTENTIONALLY LEFT BLANK

## **INITIAL DISTRIBUTION LIST**

1. Defense Technical Information Center  
Ft. Belvoir, Virginia
2. Dudley Knox Library  
Naval Postgraduate School  
Monterey, California